Improved AAVM and Small-Signal Model of Hybrid MMC Considering Dynamic Differences Between Full-Bridge and Half-Bridge Submodules

Meng Guo, Quanrui Hao, *Member, IEEE*, and Lei Ding, *Senior Member, IEEE*

***Abstract*—The hybrid modular multilevel converter (MMC), which consists of half-bridge submodules (HBSMs) and full-bridge submodules (FBSMs), is the general form of MMC. The conventional arm average value model (AAVM) of hybrid MMC assumes that the dynamics of HBSMs and FBSMs are identical and does not consider capacitor voltage differences between FBSM and HBSM, so it cannot describe the dynamics of hybrid MMC accurately. This article proposes an improved AAVM of a hybrid MMC, which includes an equivalent circuit and an arm modulation signal allocation algorithm: first, considering the dynamic difference between HBSM and FBSM, the equivalent circuit of improved AAVM was derived; second, an allocation algorithm that describes the nonlinear distribution of arm modulation signal between HBSM and FBSM was proposed. Considering the influence of high-order harmonics, the differential equation of the electrical part of hybrid MMC in the *d-q* frame was derived. Based on the nonlinear allocation algorithm of reference voltage and the piecewise solution method, the expressions of HBSM and FBSM equivalent reference voltages in the *d-q* frame were derived. A modular small-signal model of a hybrid MMC in the *d-q* frame was established. The correctness and accuracy of the proposed models are verified by simulation and experimental results.**

***Index Terms*—Arm average value model (AAVM), equivalent circuit, modular multilevel converter (MMC), small-signal model.**

I. Introduction

IN RECENT years, modular multilevel converter (MMC) has been widely used in flexible high voltage dc (HVdc) transmission technology due to its high modularity, low power loss, and low harmonic distortion [1]. MMC with half-bridge submodules (HBSMs) does not have the ability to isolate dc faults and requires dc circuit breakers to deal with dc faults [2]. The hybrid MMC with HBSM and full-bridge submodule (FBSM) has the ability to output negative voltage and ride through dc fault [3]. The hybrid MMC topology is adopted in the Kunliulong HVdc transmission project in China. The existing research mainly focuses on the design, modeling, and control methods of hybrid MMC systems. In terms of system design, Li et al. [4] studied the submodule (SM) capacitor parameter design and number configuration method. Zeng et al. [5] analyzed the voltage fluctuation characteristics of SM capacitors and proposed the design principle and voltage-sharing control strategy of SM capacitors. In [6], [7], and [8], several methods are proposed to optimize the SM capacitor parameters based on the operation constraints of hybrid MMC.

In terms of control strategies, the existing literature mainly focuses on the control methods of dc faults, which can be divided into two categories: one type of method realizes the rapid removal of dc fault current by blocking the converter, but it cannot carry out power transmission, the other method utilizes the negative voltage output capability of hybrid MMC to realize dc fault ride through [9]. In [10], the ac grid is bypassed by crossing thyristor branches to eliminate dc side and ac side current under dc short circuit fault. Psaras et al. [11] proposed a dedicated dc fault handling strategy that extended the fault clearance time. The strategy allows the use of relatively slow and cheaper dc circuit breakers and improves the fault resiliency and security of dc grids for pole-to-pole faults. Cui et al. [12] proposed a dc fault ride-through strategy in bipolar short-circuit and unipolar short-circuit scenarios based on the balancing control of arm capacitor energies. Xu et al. [3] developed a dynamic model that considered fault current commutation to accurately describe the fault-clearing process after converter blocking. The basic control of hybrid MMC includes the modulation method and capacitor voltage balance strategy [13]. Some improved phase-shift carrier pulsewidth modulation (CPS-PWM) methods have been proposed for hybrid MMC under the nominal and variable dc conditions [14], [15]. An SM capacitor voltage balance strategy is proposed based on the capacitor voltage imbalance mechanism of FBSM and HBSM under overmodulation conditions [16], [17].

In terms of analytical modeling, Dong et al. [18] proposed the analytical expression of the SM output voltage of hybrid MMC, but the second harmonic component of the arm current was not considered. A simplified arm Thévenin equivalent model for hybrid MMC is developed in [19], but the model is complex and not suitable for small-signal modeling. Lu et al. [20] proposed a conventional arm average value model (AAVM) of hybrid MMC

Manuscript received 25 September 2023; revised 9 January 2024; accepted 12 March 2024. Date of publication 19 March 2024; date of current version 16 May 2024. This work was supported by National Key R&D Program of China under Grant 2022YFB2402800. Recommended for publication by Associate Editor L. Zhang. *(Corresponding author: Quanrui Hao.)*

The authors are with the Key Laboratory of Power System Intelligent Dispatch and Control of Ministry of Education, School of Electrical Engineering, Shandong University, Jinan 250061, China (e-mail: 202014567@mail.sdu.edu.cn; haoquanrui@sdu.edu.cn; dinglei@sdu.edu.cn).

Color versions of one or more figures in this article are available at https://doi.org/10.1109/TPEL.2024.3379409.

Digital Object Identifier 10.1109/TPEL.2024.3379409

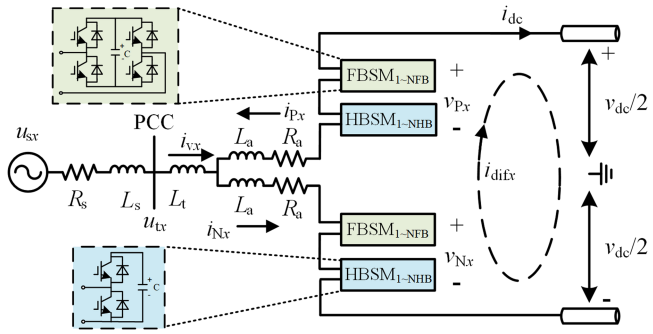

Fig. 1. Basic topology of hybrid MMC.

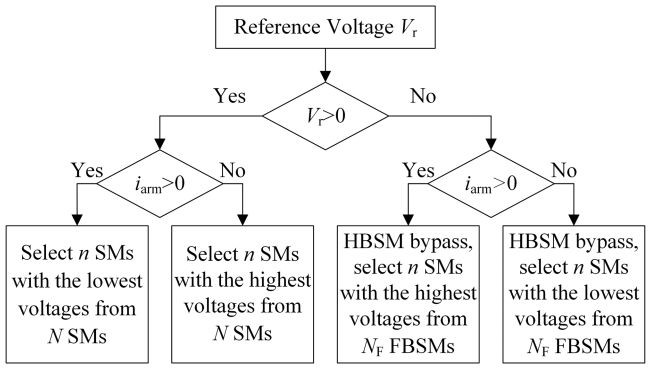

Fig. 2. Voltage balancing method of hybrid MMC.

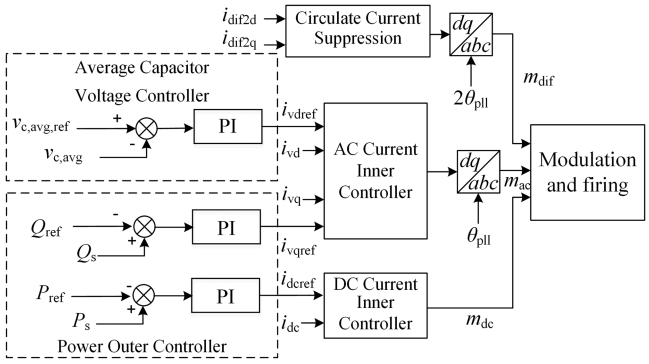

Fig. 3. Control structure of hybrid MMC.

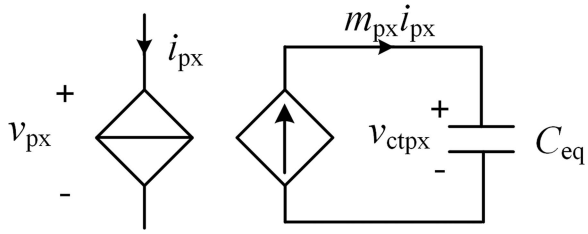

Fig. 4. Equivalent circuit of conventional AAVM.

and a calculation method for PQ operation zones considering various constraints. The existing analytical modeling studies for hybrid MMC are based on the conventional AAVM, which does not consider the difference in capacitor voltages between FBSM and HBSM under negative output voltage conditions. However, the conventional AAVM cannot accurately reflect the dynamic characteristics of hybrid MMC under some conditions, and the analysis results obtained are also quite different from the actual situation.

The novelties of this article are summarized as follows.

1) An improved AAVM of hybrid MMC based on equivalent circuit construction and arm modulation signal allocation algorithm is proposed to correctly represent the dynamic difference between HBSMs and FBSMs;
2) Based on the idea of modularization [21], the differential equations of the electrical part considering higher harmonics and the mathematical analytic expressions of arm reference voltages of FBSMs and HBSMs in the *d*-*q* frame are presented respectively, and then the complete modular small-signal models of hybrid MMC are developed.

II. Basic Principle of Hybrid MMC

The basic topology of hybrid MMC is illustrated in Fig. 1, where each arm contains N_H HBSMs and N_F FBSMs. v_{px} and v_{nx} are the output voltages of the upper and lower arms of the x phase, respectively. HBSMs can output 0 or U_c, whereas FBSMs can output $-U_c$, 0, or U_c, where U_c represents the SM capacitor voltage.

Because FBSMs can output negative voltage, hybrid MMC has a wider output range of ac voltage. The capacitor voltages of FBSMs and HBSMs within the same arm are balanced according to the principle similar to that of HBSM-MMC: the SMs with the largest voltages are switched ON when the charging current is negative, and vice versa. The difference is that the positive part of the reference voltage will be generated by FBSMs and HBSMs together, whereas the negative part of the reference voltage will be just generated by FBSMs. The details of the voltage balancing method are shown in Fig. 2.

Similar to conventional HBSM-MMC, hybrid MMC adopts the two-layer control structure including the outer and inner control loops [20]. Besides the ac current inner loop and the circulating current loop, there exists one more dc current inner loop for hybrid MMC. Typically, the outer loops are used to regulate SM average capacitor voltage $v_{c,avg}$, active power P_s, and reactive power Q_s, as shown in Fig. 3.

III. Conventional AAVM of Hybrid MMC

A. Conventional AAVM

AAVM, which ignores the voltage balancing and switching events of MMC, is the basis for deriving the small-signal model. As shown in Fig. 4, the conventional AAVM of hybrid MMC has the same circuit as that of AAVM of HBSM-MMC, which represents each arm with a controllable voltage source v_{px} that is coupled with an external circuit composed of a controllable current source and an equivalent capacitor C_{eq} [20]. The key point is that the conventional AAVM of hybrid MMC ignores dynamics differences between HBSMs and FBSMs and assumes all capacitor voltages of SMs are identical. Therefore,

$C_{eq} = C/N$, where $N = N_H + N_F$ and C is the capacitance of a single SM capacitor.

The relationship of the variables in Fig. 4 is expressed as

$$\begin{cases} C_{eq}\frac{dv_{ctpx}}{dt} = m_{px}i_{px} \\ v_{px} = m_{px}v_{ctpx} \end{cases} \quad (1)$$

where v_{ctpx} and i_{px} represent the voltage of equivalent capacitor C_{eq} and the upper arm current of phase x, and m_{px} represents the modulation signal.

According to (1), the circuit equations of the upper and lower arms of the hybrid MMC can be expressed as

$$\frac{v_{dc}}{2} - v_x = L_a\frac{di_{px}}{dt} + m_{px}v_{ctpx} + R_a i_{px} \quad (2)$$

$$\frac{v_{dc}}{2} + v_x = L_a\frac{di_{nx}}{dt} + m_{nx}v_{ctnx} + R_a i_{nx} \quad (3)$$

where v_x is ac voltage at the converter side of the transformer of phase x, and i_{px} and i_{nx} are currents of the upper and lower arm, respectively. $i_{px} = -i_{difx} - 0.5i_{vx}$ and $i_{nx} = -i_{difx} + 0.5i_{vx}$, where i_{vx} and i_{difx} represent ac current and the differential current.

Adding (2) and (3) yields

$$L_a\frac{di_{difx}}{dt} = -R_a i_{difx} + \frac{1}{2}\left(m_{px}v_{ctpx} + m_{nx}v_{ctnx}\right) - \frac{v_{dc}}{2}. \quad (4)$$

Subtracting (2) from (3) yields

$$\frac{L_a}{2}\frac{di_{vx}}{dt} = -\frac{R_a}{2}i_{vx} + \frac{1}{2}\left(m_{px}v_{ctpx} - m_{nx}v_{ctnx}\right) + v_x. \quad (5)$$

Equations (1), (4), and (5) characterize the dynamics of hybrid MMC in the *a-b-c* frame based on the conventional AAVM.

B. Defects of Conventional AAVM

The conventional AAVM of hybrid MMC is based on the premise that capacitor voltages of FBSMs and HBSMs are identical. However, the premise is only valid for the case that the arm reference voltage is positive because FBSMs and HBSMs perform the same. When the arm reference voltage is negative, the capacitor voltages of FBSMs and HBSMs are obviously different, and conventional AAVM is no longer valid.

Fig. 5 compares results from the DSM and conventional AAVM of hybrid MMC when the q-axis modulation index m_q changes from -0.5 to 0.5 at 1 s. To be noticed, there is no control implemented for hybrid MMC, and the modulation signal is directly used as input to the hybrid MMC model. As can be seen, even before 1 s, the steady-state capacitor voltage of conventional AAVM is different from DSM. After 1 s, the DSM shows that capacitor voltage gradually becomes unstable while the conventional AAVM shows it is still stable. Therefore, conventional AAVM cannot accurately reflect the dynamic of hybrid MMC in some operating conditions, because it ignores the dynamic differences between HBSM and FBSM capacitor voltages.

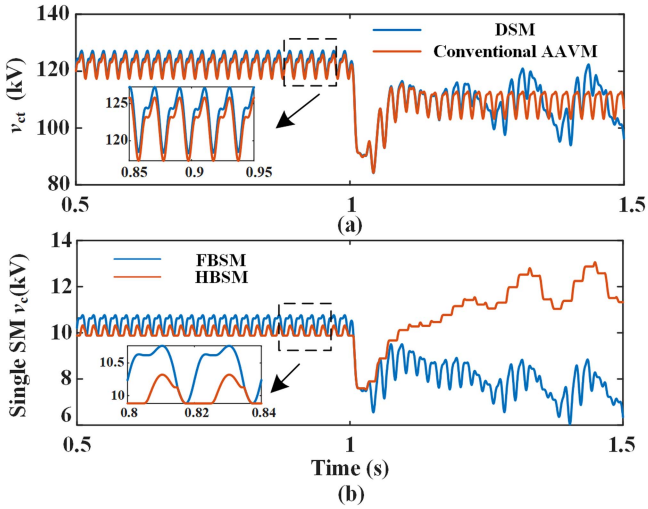

Fig. 5. Comparison of capacitor voltages. (a) Total capacitor voltages in the upper arm of DSM and conventional AAVM. (b) Single HBSM and FBSM capacitor voltages of DSM.

IV. Improved AAVM of Hybrid MMC

A. Equivalent Circuit of Improved Average Arm Model

As described above, the capacitor dynamics of HBSMs and FBSMs should be modeled separately. The proposed modeling method is based on the following assumptions.

1) One of the assumptions made in this article is that the switching frequency of hybrid MMC is high enough and the time interval of capacitor voltage balancing control is short enough. Hence, the capacitor voltages of all HBSMs are identical, and so are those of all FBSMs. Based on the assumption, the capacitor voltage sorting frequency and control time interval have no effect on the capacitor voltages of FBSMs and HBSMs. All FBSMs can be equivalent to a capacitor, and so can HBSMs.
2) The model proposed is suitable for the condition that the output voltage is generated only by FBSMs when the arm modulation signal is negative. The other possibility is that the output voltage is generated by FBSMs and HBSMs when the arm modulation signal is negative. For example, to generate $-2U_c$, the method of this article is that two FBSMs of $-U_c$ are on, and the other one is that three FBSMs of $-U_c$ and one HBSM of U_c are on. Compared with the method that the output voltage is generated by FBSMs and HBSMs, the method of this article reduces the conduction and switching losses of the SM and it has been widely used.

For each FBSM in Fig. 1

$$C_F\frac{dv_{cFj}}{dt} = S_{Fj}i_{arm} \quad (6)$$

$$v_{oFj} = S_{Fj}v_{cFj} = S_{Fj}v_{cF} \quad (7)$$

where $j = 1, 2, \ldots, N_F$ and N_F is the number of FBSMs, C_F is the capacitance of a single FBSM, i_{arm} is arm current, v_{oFj} and v_{cFj} represent output voltage and capacitor voltage of the jth

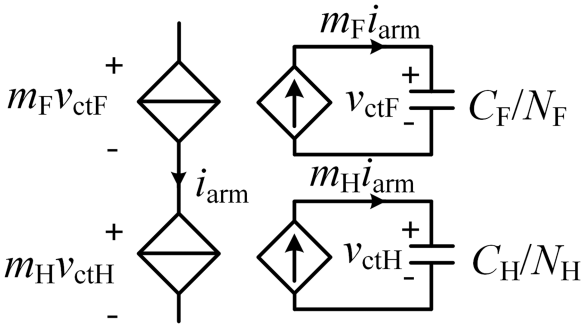

Fig. 6. Equivalent circuit of improved AAVM.

FBSM, respectively. $v_{cF1} = v_{cF2} = \ldots = v_{cFNF} = v_{cF}$. $S_{Fj} = 1$ or 0 represents the *j*th FBSM is switched ON or OFF, respectively.

Summing all equations of N_F FBSMs yields

$$C_F \frac{d}{dt}\left(\sum_{j=1}^{N_F} v_{cFj}\right) = C_F \frac{d}{dt}\left(N_F v_{cF}\right) = i_{arm} \sum_{j=1}^{N_F} S_{Fj} \tag{8}$$

$$v_{oF} = \sum_{j=1}^{N_F} v_{oFj} = v_{cF} \sum_{j=1}^{N_F} S_{Fj} \tag{9}$$

where v_{oF} represents the arm voltage generated by FBSMs. Define the modulation signal of FBSMs m_F as

$$m_F = \sum_{j=1}^{N_F} S_{Fj} \Big/ N_F. \tag{10}$$

Substituting (10) into (8) and (9) yields

$$\begin{cases} C_F \frac{d}{dt}(N_F v_{cF}) = i_{arm} m_F N_F \\ v_{oF} = m_F N_F v_{cF} \end{cases} \tag{11}$$

Since $v_{ctF} = N_F v_{cF}$, (11) can be rewritten as

$$\begin{cases} \frac{C_F}{N_F} \frac{dv_{ctF}}{dt} = m_F i_p \\ v_{oF} = m_F v_{ctF} \end{cases}. \tag{12}$$

Regardless of the high-order harmonics, $V_{SM} \Sigma S_{Fj} = V_{rFB}$, where V_{SM} is the rated capacitor voltage of a single FBSM and V_{rFB} is the reference voltage of all FBSMs. Therefore, (10) is also equal to

$$m_F = \frac{V_{rFB}}{N_F V_{SM}}. \tag{13}$$

Equations (12) and (13) constitute the AAVM of FBSMs in one arm of hybrid MMC. Similarly, the dynamics of HBSMs can be also expressed by the same equations with the symbol "H" to replace "F" in (12) and (13).

The total arm voltage of the hybrid should be the sum of the output voltages of FBSMs and HBSMs. As shown in Fig. 6, the equivalent circuit of improved AAVM consists of two series of controllable voltage sources, which represent HBSMs and FBSMs separately, instead of one identical voltage source in conventional AAVM.

B. Reference Voltage Dynamic Distribution

As shown in Fig. 6, all FBSMs and all HBSMs within one arm are considered as two separate groups. Accordingly, the arm reference voltage V_r will be divided into two parts: reference voltage V_{rFB} of the FBSM group and reference voltage V_{rHB} of the HBSM group. The corresponding voltage balancing method is shown in Fig. 2. If V_r is negative, V_r will be purely generated by the FBSM group since only FBSM can output negative voltage. If V_r is positive, V_r will be dynamically distributed between V_{rFB} and V_{rHB} depending on the arm current and the capacitor voltage.

The dynamic distribution of positive V_r between V_{rFB} and V_{rHB} follows the general principle: depending on whether arm current will charge or discharge SM capacitors, the SM group with lower or higher capacitor voltage has the priority to switch ON. For example, if a single FBSM capacitor voltage v_{cF} is smaller than a single HBSM capacitor voltage v_{cH}, FBSMs will be switched ON with the highest priority.

1) If the SM group with the highest priority cannot generate a sufficient positive voltage of V_r, all SMs of the SM group with the highest priority will switch on first and the insufficient part will be generated by the other SM group. Taking $N_H < N_F$ as an example, if V_r is bigger than $V_{cF}*N_F$, all N_F FBSMs will be switched ON and $V_r - V_{cF}*N_F$ will be generated by HBSMs, which means $V_{rFB} = V_{cF}*N_F$ and $V_{rHB} = V_r - V_{cF}*N_F$.
2) If capacitor voltages of FBSM and HBSM are equal, each SM has the same opportunity to switch on no matter if it is FBSM or HBSM. Taking $N_H < N_F$ as an example, if $v_{cF} = v_{cH}$, V_r will distribute between V_{rFB} and V_{rHB} in proportion to the number of each SM group, i.e., $V_{rFB} = V_r*N_F/(N_F + N_H)$ and $V_{rHB} = V_r*N_H/(N_F + N_H)$.
3) To avoid unnecessary switching, the tolerance ε is used to compare v_{cF} and v_{cH}. To be detailed, when $|v_{cF} - v_{cH}| < \varepsilon$, v_{cF} and v_{cH} are considered to be equal. When $v_{cF} - v_{cH} > \varepsilon$, v_{cF} is considered to be greater than v_{cH}. When $v_{cF} - v_{cH} < -\varepsilon$, v_{cF} is considered to be smaller than v_{cH}.

The details of reference voltage dynamic distribution for the case of $N_H < N_F$ are illustrated in Fig. 7. The distribution for $N_H \geq N_F$ follows a similar procedure.

C. Improved AAVM of Hybrid MMC

Based on Sections IV-A and IV-B, the completely improved AAVM shown in Fig. 8 is constituted of two components: the equivalent circuit and the reference voltage dynamic distribution logic, which is obviously different from conventional AAVM in Fig. 4. First, the arm reference voltage V_r is divided into V_{rFB} and V_{rHB} according to the procedure in Fig. 7, with the arm current and capacitor voltages of HBSM and FBSM group as the inputs. V_{rFB} and V_{rHB} are further processed to derive m_F and m_H according to (13). Finally, m_F and m_H are used as inputs to motivate the equivalent circuit.

The dynamics of hybrid MMC in the *a-b-c* frame based on the improved AAVM can be described by modifying (1), (4), and (5) based on conventional AAVM. For improved AAVM, the arm output voltage is the sum of that of HBSMs and FBSMs.

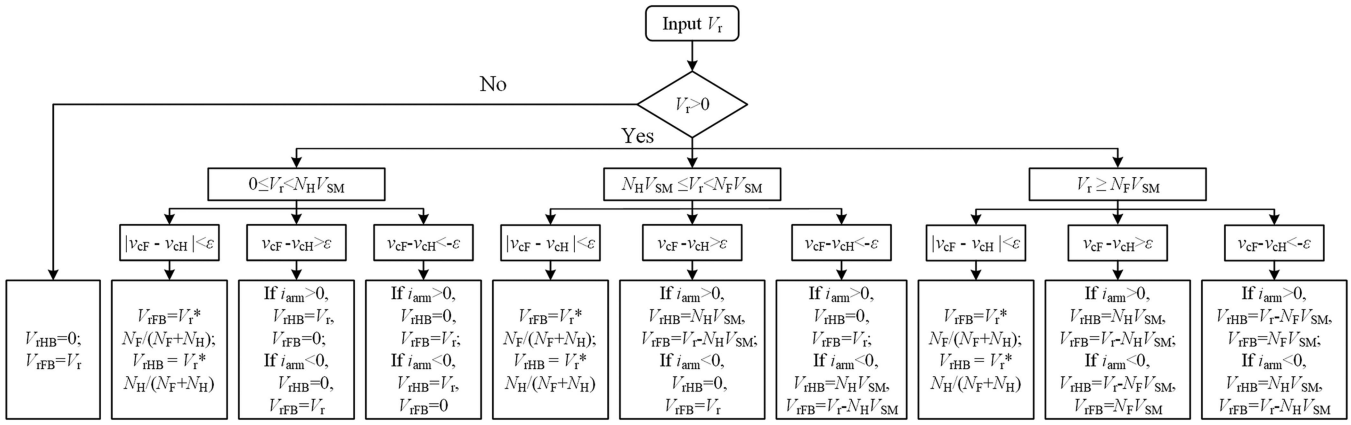

Fig. 7. Reference voltage dynamic distribution (for the case of N_H<N_F).

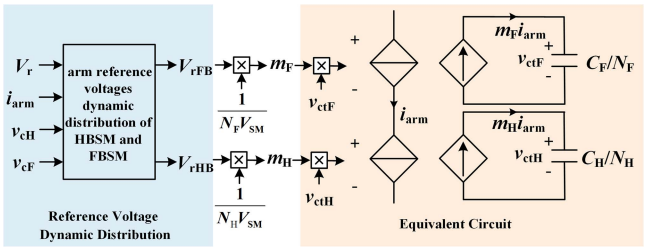

Fig. 8. Improved AAVM of hybrid MMC.

Accordingly

$$L_a \frac{di_{difx}}{dt} = -R_a i_{difx} - \frac{v_{dc}}{2} + \frac{1}{2}(m_{fpx} v_{ctfpx} + m_{fnx} v_{ctfnx} + m_{hpx} v_{cthpx} + m_{hnx} v_{cthnx}) \quad (14)$$

$$\frac{L_a}{2} \frac{di_{vx}}{dt} = v_x - \frac{R_a}{2} i_{vx} + \frac{1}{2}(m_{fpx} v_{ctfpx} - m_{fnx} v_{ctfnx} + m_{hpx} v_{cthpx} - m_{hnx} v_{cthnx}). \quad (15)$$

The dynamics of capacitor voltages of FBSMs and HBSMs are, respectively, described by

$$C_{eqF} \frac{dv_{ctfpx}}{dt} = m_{fpx}\left(-i_{difx} - \frac{i_{vx}}{2}\right) \quad (16)$$

$$C_{eqH} \frac{dv_{cthpx}}{dt} = m_{hpx}\left(-i_{difx} - \frac{i_{vx}}{2}\right) \quad (17)$$

where $C_{eqF} = C_F/N_F$ and $C_{eqH} = C_H/N_H$.

Equations (14)–(17) characterize the dynamics of hybrid MMC based on the improved AAVM. For the convenience of analysis, (14)–(17) will be transformed into the *d*-*q* frame.

D. Typical Waveforms With Improved AAVM

As shown in Fig. 9, when the arm reference voltage has a negative part, the capacitor voltage of HBSM is completely different from that of FBSM, which violates the premise of the conventional AAVM. Although the arm reference voltage is of sinusoidal waveform with dc offset, the reference voltages of HBSMs and FBSMs are irregular and nonlinear due to the dynamic distribution.

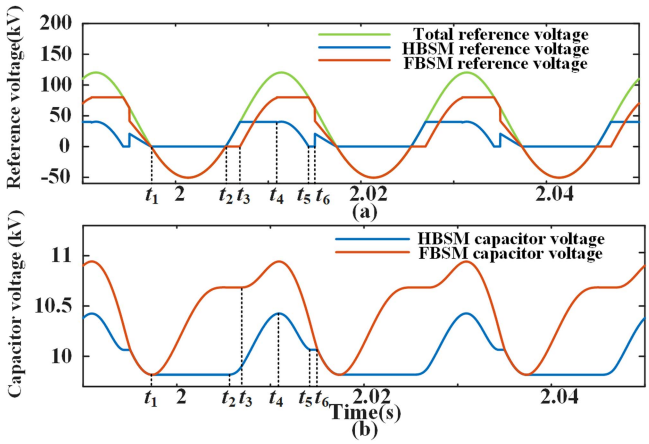

Fig. 9. Type curves of hybrid MMC improved AAVM. (a) Reference voltages. (b) Capacitor voltages.

TABLE I
COMPARISON BETWEEN IMPROVED AND CONVENTIONAL AAVM

	DSM	Improved AAVM	Conventional AAVM
Relative error	/	0.101%	4.568%
Complexity	/	Complicated	Simple
Computational time	240.0 s	10.63 s	7.53 s

E. Comparison Between Improved and Conventional AAVM

To illustrate the difference between improved AAVM and conventional AAVM, this section compares the accuracy, complexity, and computational efficiency of the two models in PSCAD. Table I shows a relative error of the total capacitor voltage v_{ct}, complexity, and computational time of the two models. The dc, fundamental-frequency (FF) and double-fundamental-frequency (DFF) components of arm reference voltage $U_{dcref} = 15$ kV, $U_{dref} = 50$ kV, $U_{qref} = -20$ kV, and $U_{2dref} = U_{2qref} = 0$ kV. The simulation time is set to 2 s, and the simulation step size and the drawing step size are both 10 μs. The computer configuration is: Win10 64-bit, i7 Intel Core CPU.

TABLE II
COMPARISON OF PRECISION UNDER DIFFERENT DC VOLTAGES

U_{dc}	Improved AAVM	Conventional AAVM
U_{dc}=15 kV(0.125U_{dcn})	0.101%	4.568%
U_{dc}=30 kV(0.25U_{dcn})	0.237%	2.552%
U_{dc}=60 kV(0.5U_{dcn})	0.064%	1.282%
U_{dc}=120 kV(U_{dcn})	0.016%	0.016%

As Table I shows, the relative error of conventional AAVM is 4.568% compared with DSM while that of improved AAVM is 0.101%. The accuracy of improved AAVM is significantly higher than that of conventional AAVM. In terms of complexity, improved AAVM is more complex due to its reference voltage dynamic distribution algorithm. Compared with DSM, the simulation time acceleration ratio of improved AAVM is 22.58 while that of conventional AAVM is 31.87. The simulation efficiencies of improved AAVM and conventional AAVM are close and much higher than DSM. It can be concluded that the complexity of improved AAVM will reduce the computational efficiency, but the reduction is within an acceptable range.

Table II shows the relative error of v_{ct} from improved AAVM and conventional AAVM under different dc voltages, $U_{dref} = 50$ kV, $U_{qref} = -20$ kV, and $U_{2dref} = U_{2qref} = 0$ kV. When the arm reference voltage exists negative part, the simulation accuracy of improved AAVM is higher than that of conventional AAVM with the decrease of dc voltage. When dc voltage is U_{dcn}, the reference voltage is all positive, and the simulation accuracy of improved AAVM is the same as that of conventional AAVM. Therefore, when hybrid MMC operates under overmodulation conditions, the larger the negative part of arm reference voltage, the more obvious the difference between FBSM and HBSM capacitor voltages, and the greater the accuracy advantage of improved AAVM.

V. SMALL-SIGNAL MODEL OF HYBRID MMC

A. Small-Signal Model of Hybrid MMC Electrical Part

For the convenience of theoretical analysis, it is better to establish the small-signal model of hybrid MMC in the *d-q* frame. The following assumptions are made for electrical and control variables for modeling: ac current i_{vx} only contains fundamental frequency component; circulating current i_{difx} contains dc and DFF components; capacitor voltages v_{ctH} and v_{ctF}, modulation signal m_H and m_F contain dc and 1–*n* harmonic components, where *n* is the highest harmonic order considered.

The *i*th harmonic of *f* can be expressed in the *d-q* frame as

$$f_i = F_{id}\cos(i\theta_{pll}) - s_i F_{iq}\sin(i\theta_{pll}) \tag{18}$$

where $s_i = 1$ when mod(i, 3) = 1 and $s_i = -1$ when mod(i, 3)≠1. The *d-q* components of the product of x_i and y_j can also be expressed by *d-q* components of x_i and y_j in a general form of

$$\begin{aligned}(x_i y_j)_{(i+j)d} &= 0.5\left(X_{id}Y_{jd} - s_i s_j X_{iq}Y_{jq}\right)\\ (x_i y_j)_{(i+j)q} &= 0.5 s_{i+j}\left(s_i X_{iq}Y_{jd} + s_j X_{id}Y_{jq}\right)\\ (x_i y_j)_{(i-j)d} &= 0.5\left(X_{id}Y_{jd} + s_i s_j X_{iq}Y_{jq}\right)\\ (x_i y_j)_{(i-j)q} &= 0.5 s_{i-j}\left(s_i X_{iq}Y_{jd} - s_j X_{id}Y_{jq}\right).\end{aligned} \tag{19}$$

Based on (19), the differential equations in (14)–(17) of the improved AAVM in the *a-b-c* frame can be mapped into the *d-q* frame. Based on that, the small-signal model of the electric part can be expressed as

$$\begin{cases}\Delta\dot{\boldsymbol{x}}_e = \boldsymbol{A}_e\Delta\boldsymbol{x}_e + \boldsymbol{B}_{em}\Delta\boldsymbol{m}_{f,h} + \boldsymbol{B}_{euw}\Delta\boldsymbol{u}_{ew} + \boldsymbol{B}_{eur}\Delta\boldsymbol{u}_{er}\\ \Delta\boldsymbol{y}_e = \boldsymbol{C}_e\Delta x_e + \boldsymbol{D}_{em}\Delta\boldsymbol{m}_{f,h} + \boldsymbol{D}_{euw}\Delta\boldsymbol{u}_{ew} + \boldsymbol{D}_{eur}\Delta\boldsymbol{u}_{er}\end{cases} \tag{20}$$

where $\Delta\boldsymbol{x}_e = [\Delta i_{diff0}, \Delta i_{vd}, \Delta i_{vq}, \Delta i_{dif2d}, \Delta i_{dif2q}, \Delta v_{c0f}, \Delta v_{c1df}, \ldots, \Delta v_{cndf}, \Delta v_{c1qf}, \ldots, \Delta v_{cnqf}, \Delta v_{c0h}, \Delta v_{c1dh}, \ldots, \Delta v_{cndh}, \Delta v_{c1qh}, \ldots, \Delta v_{cnqh}]^T$, $\Delta\boldsymbol{m}_{f,h} = [\Delta m_{0f}, \Delta m_{1df}, \ldots, \Delta m_{ndf}, \Delta m_{1qf}, \ldots, \Delta m_{nqf}, \Delta m_{0h}, \Delta m_{1dh}, \ldots, \Delta m_{ndh}, \Delta m_{1qh}, \ldots\Delta m_{nqh}]^T$, $\Delta\boldsymbol{u}_{er} = [\Delta v_{sd}, \Delta v_{sq}, \Delta v_{dc}]^T$, $\Delta\boldsymbol{u}_{ew} = [\Delta\omega, \Delta\theta_{pll}]^T$, and $\Delta\boldsymbol{y}_e = [\Delta v_{td}, \Delta v_{tq}, \Delta v_{dc}, \Delta i_{dc}, \Delta i_{vd}, \Delta i_{vq}, \Delta i_{dif2d}, \Delta i_{dif2q}, \Delta v_{c,avg}]^T$. Δi_{dif0}, Δi_{dif2d}, and Δi_{dif2q} are dc and DFF-dq components of circulating current, Δi_{vd} and Δi_{vq} are *d-q* components of ac current, and Δv_{c0f}, Δv_{c1df}, …, Δv_{cndf}, and Δv_{c1qf}, …, Δv_{cnqf} are dc and *d-q* components of FBSM capacitor voltage. Δm_{0f}, Δm_{1df}, …, Δm_{ndf}, and Δm_{1qf}, …, Δm_{nqf} are dc and *d-q* components of the modulation signal of FBSMs, and the variables for HBSMs are named in the same way. Δv_{sd} and Δv_{sq} are *d-q* components of ac voltage.

B. Small-Signal Model of Reference Voltage Distribution

According to the reference voltage dynamic distribution in Section III-B, it is difficult to directly derive its expression in the *d-q* frame with the approach in Section V-A because reference voltages for HBSMs and FBSMs are irregular and highly nonlinear, as shown in Fig. 9. In this section, a piecewise method is proposed to derive the mathematical expression of reference voltage distribution in the *d-q* frame.

Since the reference voltage distribution contains a logical judgment part, the state-space model cannot be established. Therefore, using the idea of small-signal modeling, the small-signal model of reference voltage distribution can be written as

$$\Delta\boldsymbol{m}_{f,h} = \boldsymbol{C}_T\Delta\boldsymbol{x}_e + \boldsymbol{D}_{Tm}\Delta\boldsymbol{m} + \boldsymbol{D}_{Tu}\Delta\boldsymbol{u}_{ew} \tag{21}$$

where $\Delta\boldsymbol{m} = [\Delta m_{dc}, \Delta m_d, \Delta m_q, \Delta m_{2d}, \Delta m_{2q}]^T$ represents modulation index of MMC. The subscript "dc," "1," and "2" represent the dc, FF, and DFF components of the modulation index.

Take the modulation signal m_f of FBSMs as an example. According to the Fourier transformation, the harmonics of m_f can be calculated by

$$m_{0f} = \frac{1}{T}\int_{t_1}^{t_1+T} m_f dt \tag{22}$$

$$m_{ndf} = \frac{2}{T}\int_{t_1}^{t_1+T} m_f\cos n\theta_{pll} dt \tag{23}$$

$$m_{nqf} = \frac{2s_n}{T}\int_{t_1}^{t_1+T} m_f\sin n\theta_{pll} dt. \tag{24}$$

The above equations also apply to the harmonics of $m_{\rm h}$ for HBSMs just by replacing the subscript "f" with "h." As shown in Fig. 9, reference voltages of HBSMs and FBSMs are linear within specific time intervals defined by instants t_1–t_6. The time instants t_1-t_6 are defined as follows:

t_1: First zero-crossing point of $V_{\rm r}$;
t_2: Second zero-crossing point of $V_{\rm r}$;
t_3: First zero-crossing point of $V_{\rm r} - N_{\rm H}V_{\rm SM}$;
t_4: Zero-crossing point of $i_{\rm arm}$ at $V_{\rm r}>0$;
t_5: Second zero-crossing point of $V_{\rm r} - N_{\rm F}V_{\rm SM}$;
t_6: First intersection time of $v_{\rm cf}$ and $v_{\rm ch}$.

Therefore, $V_{\rm rFB}$ within a period can be described as: $V_{\rm rFB} = V_{\rm r}$ when $t_1<t\le t_2$; $V_{\rm rFB} = 0$ when $t_2<t\le t_3$; $V_{\rm rFB} = V_{\rm r} - N_{\rm H}V_{\rm SM}$ when $t_3<t\le t_4$; $V_{\rm rFB} = N_{\rm F}V_{\rm SM}$ when $t_4<t\le t_5$; $V_{\rm rFB} = V_{\rm r}$ when $t_5<t\le t_6$; and $V_{\rm rFB} = V_{\rm r}N_{\rm F}/N$ when $t_6<t\le t_1+T$. Thus, (22) can be rewritten as the sum of multiple interval integrals

$$m_{0\rm f} = \frac{1}{TN_{\rm F}V_{\rm csm}}\left[\int_{t_1}^{t_2} V_{\rm r}dt + \int_{t_3}^{t_4}(V_{\rm r} - N_{\rm H}V_{\rm SM})\,dt + \int_{t_4}^{t_5} N_{\rm F}V_{\rm SM}dt + \int_{t_5}^{t_6} V_{\rm r}dt + \int_{t_6}^{t_1+T}\frac{N_{\rm F}}{N}V_{\rm r}dt\right] \tag{25}$$

where $V_{\rm r} = 0.5u_{\rm dcn}(m_{\rm dc} - m_{\rm d}\cos\theta_{\rm pll} + m_{\rm q}\sin\theta_{\rm pll} - m_{\rm 2d}\cos 2\theta_{\rm pll} - m_{\rm 2q}\sin 2\theta_{\rm pll})$, and $u_{\rm dcn}$ is the nominal dc voltage. Equations (23) and (24) can also be rewritten as the sum of multiple interval integrals and the expression of HBSM can be obtained by replacing the subscript "f" with "h."

According to the meaning of each segment time, the corresponding functions of segment time are shown in the following equations:

$$t_1:\ V_{\rm r}(t_1) = \tfrac{u_{\rm dcn}}{2}(m_{\rm dc} - m_{\rm d}\cos\theta_{\rm pll}(t_1) + m_{\rm q}\sin\theta_{\rm pll}(t_1) - m_{\rm 2d}\cos 2\theta_{\rm pll}(t_1) - m_{\rm 2q}\sin 2\theta_{\rm pll}(t_1)) = 0 \tag{26}$$

$$t_2:\ V_{\rm r}(t_2) = \tfrac{u_{\rm dcn}}{2}(m_{\rm dc} - m_{\rm d}\cos\theta_{\rm pll}(t_2) + m_{\rm q}\sin\theta_{\rm pll}(t_2) - m_{\rm 2d}\cos 2\theta_{\rm pll}(t_2) - m_{\rm 2q}\sin 2\theta_{\rm pll}(t_2)) = 0 \tag{27}$$

$$t_3:\ V_{\rm r}(t_3) - N_{\rm H}V_{\rm SM} = \tfrac{u_{\rm dcn}}{2}(m_{\rm dc} - m_{\rm d}\cos\theta_{\rm pll}(t_3) + m_{\rm q}\sin\theta_{\rm pll}(t_3) - m_{\rm 2d}\cos 2\theta_{\rm pll}(t_3) - m_{\rm 2q}\sin 2\theta_{\rm pll}(t_3)) - N_{\rm H}V_{\rm SM} = 0 \tag{28}$$

$$t_4:\ i_{\rm arm}(t_4) = -i_{\rm dif0} - 0.5i_{\rm vd}\cos\theta_{\rm pll}(t_4) + 0.5i_{\rm vq}\sin\theta_{\rm pll}(t_4) - i_{\rm dif2d}\cos 2\theta_{\rm pll}(t_4) - i_{\rm dif2q}\sin 2\theta_{\rm pll}(t_4) = 0 \tag{29}$$

$$t_5:\ V_{\rm r}(t_5) - N_{\rm F}V_{\rm SM} = \tfrac{u_{\rm dcn}}{2}(m_{\rm dc} - m_{\rm d}\cos\theta_{\rm pll}(t_5) + m_{\rm q}\sin\theta_{\rm pll}(t_5) - m_{\rm 2d}\cos 2\theta_{\rm pll}(t_5) - m_{\rm 2q}\sin 2\theta_{\rm pll}(t_5)) - N_{\rm F}V_{\rm SM} = 0 \tag{30}$$

$$t_6:\ v_{\rm cf}(t_6) - v_{\rm ch}(t_6) = \tfrac{1}{N_{\rm F}}\left[v_{\rm c0f} + \textstyle\sum_{i=1}^{n}(v_{\rm cidf}\cos\theta_{\rm pll}(t_6) - s_{\rm i}v_{\rm ciqf}\sin\theta_{\rm pll}(t_6))\right] - \tfrac{1}{N_{\rm H}}\left[v_{\rm c0h} + \textstyle\sum_{i=1}^{n}(v_{\rm cidh}\cos\theta_{\rm pll}(t_6) - s_{\rm i}v_{\rm ciqh}\sin\theta_{\rm pll}(t_6))\right] = 0 \tag{31}$$

where the subscript "i" represents the ith harmonic component of the capacitor voltage.

According to (25), the analytical expression of the modulation signal $\boldsymbol{m}_{\rm f,h}$ contains $\boldsymbol{m}$, the segment time vector $\boldsymbol{t}_{\rm m}$, and $\boldsymbol{u}_{\rm ew}$, where $\boldsymbol{t}_{\rm m} = [t_1, t_2, t_3, t_4, t_5, t_6]^{\rm T}$. The function relationship can be written as

$$\boldsymbol{m}_{\rm f,h} = \boldsymbol{f}_1(\boldsymbol{m}, \boldsymbol{t}_{\rm m}, \boldsymbol{u}_{\rm ew}). \tag{32}$$

According to (26)–(31), the function relationship between $\boldsymbol{t}_{\rm m}$, $\boldsymbol{m}$, $\boldsymbol{x}_{\rm e}$, and $\boldsymbol{u}_{\rm ew}$ can be written as

$$\boldsymbol{f}_2(\boldsymbol{m}, \boldsymbol{t}_{\rm m}, \boldsymbol{x}_{\rm e}, \boldsymbol{u}_{\rm ew}) = 0. \tag{33}$$

By linearizing (32) at a steady-state point, the expression of $\Delta\boldsymbol{m}_{\mathbf{f,h}}$ can be written as

$$\Delta\boldsymbol{m}_{\rm f,h} = \frac{\partial\boldsymbol{f}_1}{\partial\boldsymbol{m}}\Delta\boldsymbol{m} + \frac{\partial\boldsymbol{f}_1}{\partial\mathbf{t}_{\boldsymbol{m}}}\Delta\boldsymbol{t}_{\boldsymbol{m}} + \frac{\partial\boldsymbol{f}_1}{\partial\mathbf{u}_{\rm ew}}\Delta\boldsymbol{u}_{\rm ew}. \tag{34}$$

Similarly, according to the implicit function differentiation rule, $\Delta\boldsymbol{t}_{\mathbf{m}}$ can be written as

$$\Delta\boldsymbol{t}_{\rm m} = -\frac{\partial\boldsymbol{f}_2/\partial\boldsymbol{x}_{\rm e}}{\partial\boldsymbol{f}_2/\partial\boldsymbol{t}_{\rm m}}\Delta\boldsymbol{x}_{\rm e} - \frac{\partial\boldsymbol{f}_2/\partial\boldsymbol{m}}{\partial\boldsymbol{f}_2/\partial\mathbf{t}_{\rm m}}\Delta\mathbf{m} - \frac{\partial\boldsymbol{f}_2/\partial\boldsymbol{u}_{\rm ew}}{\partial\boldsymbol{f}_2/\partial\boldsymbol{t}_{\rm m}}\Delta\boldsymbol{u}_{\rm ew}. \tag{35}$$

Substituting (34) into (35), the expression of $\boldsymbol{C}_{\rm T}$, $\boldsymbol{D}_{\rm Tm}$, and $\boldsymbol{D}_{\rm Tu}$ in (21) can be written as

$$\begin{aligned}\boldsymbol{C}_{\rm T} &= \frac{\partial\boldsymbol{f}_1}{\partial\boldsymbol{t}_{\rm m}}\left(-\frac{\partial\boldsymbol{f}_2}{\partial\boldsymbol{x}_{\rm e}}\Big/\frac{\partial\boldsymbol{f}_2}{\partial\boldsymbol{t}_{\rm m}}\right)\\ \boldsymbol{D}_{\rm Tm} &= \frac{\partial\boldsymbol{f}_1}{\partial\boldsymbol{m}} + \frac{\partial\boldsymbol{f}_1}{\partial\boldsymbol{t}_{\rm m}}\left(-\frac{\partial\boldsymbol{f}_2}{\partial\boldsymbol{m}}\Big/\frac{\partial\boldsymbol{f}_2}{\partial\boldsymbol{t}_{\rm m}}\right)\\ \boldsymbol{D}_{\rm Tu} &= \frac{\partial\boldsymbol{f}_1}{\partial\boldsymbol{u}_{\rm ew}} + \frac{\partial\boldsymbol{f}_1}{\partial\boldsymbol{t}_{\rm m}}\left(-\frac{\partial\boldsymbol{f}_2}{\partial\boldsymbol{u}_{\rm ew}}\Big/\frac{\partial\boldsymbol{f}_2}{\partial\boldsymbol{t}_{\rm m}}\right)\end{aligned} \tag{36}$$

where $\boldsymbol{C}_{\rm T}$ is a $(4n+2)\times(4n+7)$-dimensional matrix, $\boldsymbol{D}_{\rm Tm}$ is a $(4n+2)\times 5$-dimensional matrix, and $\boldsymbol{D}_{\rm Tu}$ is a $(4n+2)\times 5$-dimensional matrix (n is the order of harmonics considered).

C. Small-Signal Model of Hybrid MMC With Control System

The small-signal model of the electrical part is as follows:

$$\begin{cases}\Delta\dot{\boldsymbol{x}}_{\rm s} = \boldsymbol{A}_{\rm s}\Delta\boldsymbol{x}_{\rm s} + \boldsymbol{B}_{\rm sc}\Delta\boldsymbol{u}_{\rm sc} + \boldsymbol{B}_{\rm sr}\Delta\boldsymbol{u}_{\rm sr}\\ \Delta\boldsymbol{y}_{\rm s} = \boldsymbol{C}_{\rm s}\Delta\boldsymbol{x}_{\rm s} + \boldsymbol{D}_{\rm sc}\Delta\boldsymbol{u}_{\rm sc} + \boldsymbol{D}_{\rm sr}\Delta\boldsymbol{u}_{\rm sr}\end{cases} \tag{37}$$

where $\Delta\boldsymbol{x}_{\rm s} = \Delta\boldsymbol{x}_{\rm e}$, $\Delta\boldsymbol{u}_{\rm sc} = [\Delta\boldsymbol{m}; \Delta\boldsymbol{u}_{\rm ew}]$, $\Delta\boldsymbol{u}_{\rm sr} = \Delta\boldsymbol{u}_{\rm er}$, and $\Delta\boldsymbol{y}_{\rm s} = \Delta\boldsymbol{y}_{\rm e}$.

Therefore

$$\begin{cases} \boldsymbol{A}_{\mathrm{s}} = \boldsymbol{A}_{\mathrm{e}} + \boldsymbol{B}_{\mathrm{em}}\boldsymbol{C}_{\mathrm{T}} \\ \boldsymbol{B}_{\mathrm{sc}} = \begin{bmatrix} \boldsymbol{B}_{\mathrm{em}}\boldsymbol{D}_{\mathrm{Tm}} & \boldsymbol{0} \\ \boldsymbol{0} & \boldsymbol{B}_{\mathrm{euw}} + \boldsymbol{B}_{\mathrm{em}}\boldsymbol{D}_{\mathrm{Tu}} \end{bmatrix}, \boldsymbol{B}_{\mathrm{sr}} = \boldsymbol{B}_{\mathrm{eur}} \\ \boldsymbol{C}_{\mathrm{s}} = \boldsymbol{C}_{\mathrm{e}} + \boldsymbol{D}_{\mathrm{em}}\boldsymbol{C}_{\mathrm{T}} \\ \boldsymbol{D}_{\mathrm{sc}} = \begin{bmatrix} \boldsymbol{D}_{\mathrm{em}}\boldsymbol{D}_{\mathrm{Tm}} & \boldsymbol{0} \\ \boldsymbol{0} & \boldsymbol{D}_{\mathrm{euw}} + \boldsymbol{D}_{\mathrm{em}}\boldsymbol{D}_{\mathrm{Tu}} \end{bmatrix}, \boldsymbol{D}_{\mathrm{sr}} = \boldsymbol{D}_{\mathrm{eur}} \end{cases}. \tag{38}$$

The control system considers the inner and outer loop and phase-locked loop (PLL) controller. Based on [20], the small-signal model of the control system is established as follows:

$$\begin{cases} \Delta\dot{\boldsymbol{x}}_{\mathrm{c}} = \boldsymbol{A}_{\mathrm{c}}\Delta\boldsymbol{x}_{\mathrm{c}} + \boldsymbol{B}_{\mathrm{c1}}\Delta\boldsymbol{u}_{\mathrm{c1}} + \boldsymbol{B}_{\mathrm{c2}}\Delta\boldsymbol{u}_{\mathrm{c2}} \\ \Delta\boldsymbol{y}_{\mathrm{c}} = \boldsymbol{C}_{\mathrm{c}}\Delta\boldsymbol{x}_{\mathrm{c}} + \boldsymbol{D}_{\mathrm{c1}}\Delta\boldsymbol{u}_{\mathrm{c1}} + \boldsymbol{D}_{\mathrm{c2}}\Delta\boldsymbol{u}_{\mathrm{c2}} \end{cases} \tag{39}$$

where $\Delta\boldsymbol{x}_{\mathrm{c}} = [\Delta\theta_{\mathrm{pll}}, \Delta x_{\mathrm{pll}}, \Delta x_{\mathrm{P}}, \Delta x_{\mathrm{Q}}, \Delta x_{\mathrm{dc}}, \Delta x_{\mathrm{id}}, \Delta x_{\mathrm{iq}}, \Delta x_{\mathrm{idc}}, \Delta x_{2\mathrm{d}}, \Delta x_{2\mathrm{q}}]^{\mathrm{T}}$, $\Delta\boldsymbol{u}_{\mathrm{c1}} = [\Delta P_{\mathrm{ref}}, \Delta Q_{\mathrm{ref}}, \Delta v_{\mathrm{c,avg,ref}}]^{\mathrm{T}}$, $\Delta\boldsymbol{u}_{\mathrm{c2}} = \Delta\boldsymbol{y}_{\mathrm{s}}$, and $\Delta\boldsymbol{y}_{\mathrm{c}} = \Delta\boldsymbol{u}_{\mathrm{sc}}$. The small-signal model of the inverter station control system can be obtained by replacing Δx_{P} and ΔP_{ref} with the dc voltage outer loop control variables Δx_{dc} and $\Delta v_{\mathrm{dcref}}$.

By linearizing at the steady-state point, the small-signal model of hybrid MMC with control and ac system can be written as

$$\begin{cases} \Delta\dot{\boldsymbol{x}}_{\mathrm{sys}} = \boldsymbol{A}_{\mathrm{sys}}\Delta\boldsymbol{x}_{\mathrm{sys}} + \boldsymbol{B}_{\mathrm{sys}}\Delta\boldsymbol{u}_{\mathrm{sys}} \\ \Delta\boldsymbol{y}_{\mathrm{sys}} = \boldsymbol{C}_{\mathrm{sys}}\Delta\boldsymbol{x}_{\mathrm{sys}} \end{cases} \tag{40}$$

where $\Delta\boldsymbol{x}_{\mathrm{sys}} = [\Delta x_{\mathrm{s}}; \Delta x_{\mathrm{c}}]$, $\Delta\boldsymbol{u}_{\mathrm{sys}} = [\Delta\boldsymbol{u}_{\mathrm{sr}}; \Delta\boldsymbol{u}_{\mathrm{c1}}]$, and $\Delta\boldsymbol{y}_{\mathrm{sys}} = \Delta\boldsymbol{x}_{\mathrm{sys}}$.

Therefore

$$\begin{cases} \boldsymbol{A}_{\mathrm{sys}} = \\ \begin{bmatrix} \boldsymbol{A}_{\mathrm{s}} + \boldsymbol{B}_{\mathrm{sc}}\boldsymbol{D}_{\mathrm{c2}}\boldsymbol{H}_1\boldsymbol{C}_{\mathrm{s}} & \boldsymbol{B}_{\mathrm{sc}}(\boldsymbol{E} + \boldsymbol{D}_{\mathrm{c2}}\boldsymbol{H}_1\boldsymbol{D}_{\mathrm{sc}})\boldsymbol{C}_{\mathrm{c}} \\ \boldsymbol{B}_{\mathrm{c2}}(\boldsymbol{E} + \boldsymbol{D}_{\mathrm{sc}}\boldsymbol{H}_2\boldsymbol{D}_{\mathrm{c2}})\boldsymbol{C}_{\mathrm{s}} & \boldsymbol{A}_{\mathrm{c}} + \boldsymbol{B}_{\mathrm{c2}}\boldsymbol{D}_{\mathrm{sc}}\boldsymbol{H}_2\boldsymbol{C}_{\mathrm{c}} \end{bmatrix} \\ \boldsymbol{B}_{\mathrm{sys}} = \\ \begin{bmatrix} \boldsymbol{B}_{\mathrm{sr}} + \boldsymbol{B}_{\mathrm{sc}}\boldsymbol{D}_{\mathrm{c2}}\boldsymbol{H}_1\boldsymbol{D}_{\mathrm{sr}} & \boldsymbol{B}_{\mathrm{sc}}(\boldsymbol{E} + \boldsymbol{D}_{\mathrm{c2}}\boldsymbol{H}_1\boldsymbol{D}_{\mathrm{sc}})\boldsymbol{D}_{\mathrm{c1}} \\ \boldsymbol{B}_{\mathrm{c2}}(\boldsymbol{E} + \boldsymbol{D}_{\mathrm{sc}}\boldsymbol{H}_2\boldsymbol{D}_{\mathrm{c2}})\boldsymbol{D}_{\mathrm{sr}} & \boldsymbol{B}_{\mathrm{c1}} + \boldsymbol{B}_{\mathrm{c2}}\boldsymbol{D}_{\mathrm{sc}}\boldsymbol{H}_2\boldsymbol{D}_{\mathrm{c1}} \end{bmatrix} \\ \boldsymbol{C}_{\mathrm{sys}} = \boldsymbol{E} \end{cases} \tag{41}$$

where

$$\begin{cases} \boldsymbol{H}_1 = (\boldsymbol{E} - \boldsymbol{D}_{\mathrm{sc}}\boldsymbol{D}_{\mathrm{c2}})^{-1} \\ \boldsymbol{H}_2 = (\boldsymbol{E} - \boldsymbol{D}_{\mathrm{c2}}\boldsymbol{D}_{\mathrm{sc}})^{-1} \end{cases}. \tag{42}$$

VI. Simulation Verification

A. Parameters of Test System

Taking the test system shown in Fig. 10, for example, DSM, the conventional AAVM, and the improved AAVM proposed in this article are constructed in PSCAD. According to the configuration principle of SMs for hybrid MMC in [22] and [23], the ratio between FBSMs and HBSMs numbers is set to 2:1. Parameters of the test system are shown in Table III.

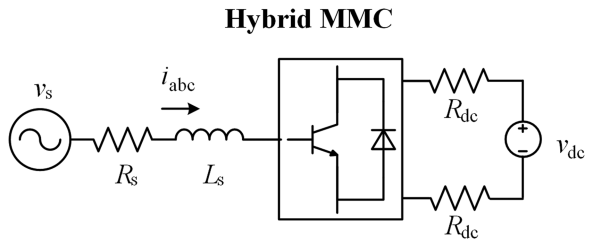

Fig. 10. Topology of the test system.

TABLE III
Parameter of Hybrid MMC Test System

Circuit parameter of hybrid MMC					
V_{s} /kV	70	L_{t} /mH	15	R_{a} /Ω	1.0
L_{s} /mH	11	L_{a} /mH	24	SM No. (FBSM/HBSM)	8/4
R_{s} /Ω	0.62	V_{dcn}/kV	±60	C_{sm}/μF	9000
Control parameter of hybrid MMC					
ac ILCC PI	4, 100	power PI	0.3,100	PLL PI	200,1000
dc ILCC PI	5.4,11.1	CCSC PI	15,2000	$v_{\mathrm{c,avg}}$ PI	4,100

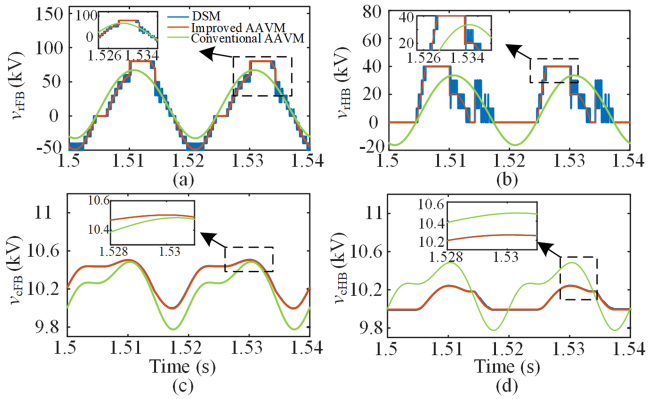

Fig. 11 Steady-state curves of different models. (a) Reference voltage of FBSM. (b) Reference voltage of HBSM. (c) Capacitor voltage of FBSM. (d) Capacitor voltage of HBSM.

B. Accuracy Verification of Improved AAVM

To verify the accuracy of the improved AAVM, this section compares the DSM, the conventional AAVM, and the improved AAVM under open loop mode in PSCAD. Fig. 11(a) and (b) shows that, without considering the high-order switching harmonics of the reference voltages for DSM due to the switching process, the reference voltages of improved AAVM are consistent with that of DSM. The reference voltages of conventional AAVM are obviously different from the DSM. As shown in Fig. 11(c) and (d), the capacitor voltages of HBSM and FBSM from improved AAVM are highly consistent with that of DSM while the capacitor voltages of conventional AAVM exist errors compared with DSM. Fig. 12 compares the transient response of different models. Before 1 s, $m_{\mathrm{dc}} = 0.5$, $m_{\mathrm{d}} = 1.2$, $m_{\mathrm{q}} = -0.33$, and $m_{2\mathrm{d}} = m_{2\mathrm{q}} = 0.05$. At 1 s, m_{q} changes from – 0.33 to 0.67. The SM total capacitor voltage and the arm current of the DSM are unstable after 1 s. The improved AAVM transient response is

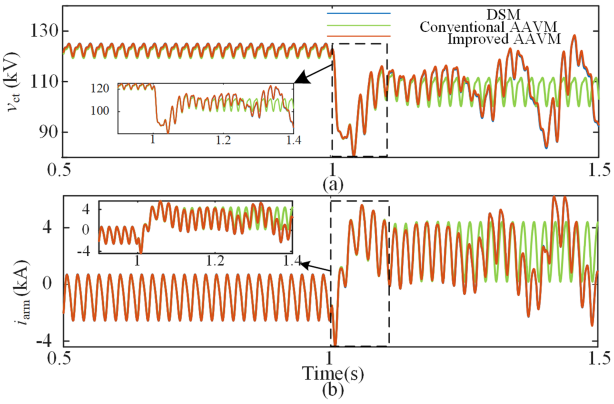

Fig. 12. Transient response curves of different models. (a) Total capacitor voltage. (b) Current in upper arm.

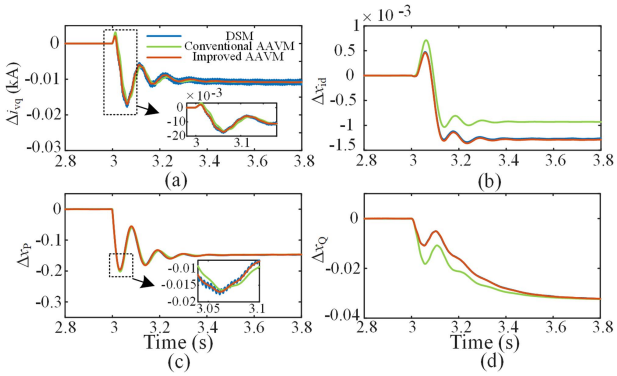

Fig. 13. Small-signal dynamics of different models. (a) Δi_{vq}. (b) Δx_{id}. (c) Δx_{P}. (d) Δx_{Q}.

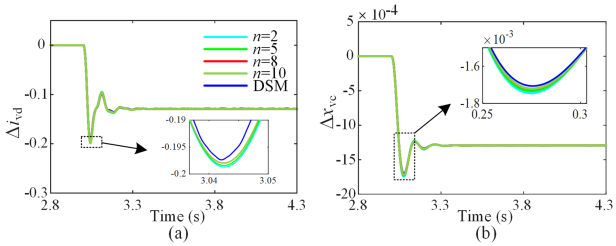

Fig. 14. Small-signal dynamics with different harmonic orders.

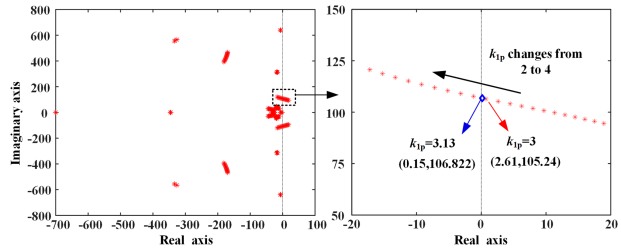

Fig. 15. Root locus of the conventional AAVM as $k_{1\mathrm{p}}$ changes from 2 to 4.

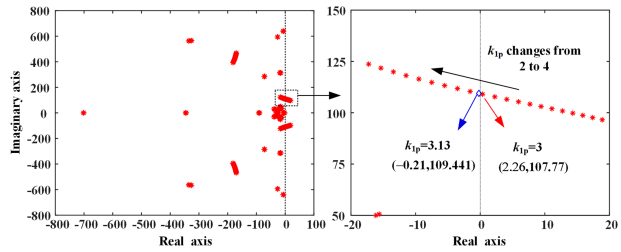

Fig. 16. Root locus of the improved AAVM as $k_{1\mathrm{p}}$ changes from 2 to 4.

consistent with that of DSM, whereas the conventional AAVM remains stable. Therefore, the improved AAVM can predict the dynamic characteristics of hybrid MMC correctly and accurately than the conventional AAVM.

C. Small-Signal Dynamics and Stability of Hybrid MMC

According to the small-signal modeling method proposed in Section V, the small-signal dynamics of conventional AAVM and improved AAVM are simulated in MATLAB. The small-signal dynamics of DSM are also simulated in PSCAD. At 3 s, P_{ref} changes from 220 to 210 MW. Fig. 13 illustrates the small-signal dynamics of Δi_{vd}, Δx_{id}, Δx_{P}, and Δx_{Q} from three models. As can be observed, the small-signal dynamics of improved AAVM are consistent with DSM in PSCAD. Although Δi_{vd} of the conventional AAVM is close to the DSM, Δx_{id}, Δx_{P}, and Δx_{Q} of the conventional AAVM are obviously different from the DSM. It can be concluded that the improved AAVM can correctly simulate the small-signal dynamics of DSM.

To reflect the influence of different harmonic orders on small-signal model accuracy, this section compares the dynamic responses of the small-signal model with harmonics up to various orders. At 3 s, P_{ref} changes from 220 to 210 MW. Fig. 14 shows the small-signal dynamics of Δi_{vd} and Δx_{vc} with harmonics up to the order of 2, 5, 8, and 10. It can be seen that the accuracy of the small-signal model is higher with the increase of harmonic order. The small-signal dynamics corresponding to $n = 8$ and $n = 10$ are very close. With the increase of the harmonic order, the dimension of the system matrix and the calculation time also increase. To balance the computational efficiency and accuracy of the proposed model, this article considers the harmonics up to the order of $n = 8$.

The small-signal stability of the hybrid MMC can be evaluated by calculating the eigenvalues of the systematic matrix A_{sys} in (40). $k_{1\mathrm{p}}$ is the proportional parameter of the ac current inner loop, and many literatures have selected $k_{1\mathrm{p}}$ as the parameter to show the results. Therefore, $k_{1\mathrm{p}}$ is selected as the parameter to show the results in this article. Figs. 15 and 16 show the root loci of conventional AAVM and improved AAVM as the proportional parameter $k_{1\mathrm{p}}$ of ac current inner loop changes from 2 to 4 with the step of 0.1. In Figs. 15 and 16, two branches of the root loci, which are considered the dominant roots, start to move to the left half plane as $k_{1\mathrm{p}}$ increases. The loci of the dominant roots are zoomed in at the right sides of Figs. 15 and 16.

It can be observed from Fig. 15 that the critical value of $k_{1\mathrm{p}}$ is around 3.14. When $k_{1\mathrm{p}}$ is less than 3.14, the dominant root will be located in the right half plane, which indicates that the test system becomes unstable based on the conventional AAVM. In Fig. 15, the eigenvalue of the dominant root for $k_{1\mathrm{p}} = 3.13$ are $0.15 \pm j106.82$ and $k_{1\mathrm{p}} = 3$ are $2.61 \pm j105.64$.

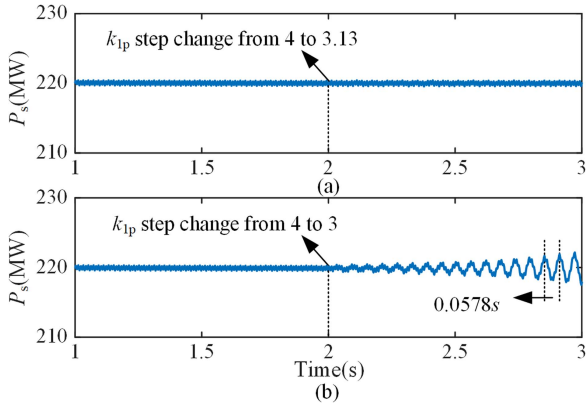

Fig. 17. Dynamics of active power with different k_{1p} changing at $t = 2$ s. (a) k_{1p} changes from 4 to 3.13. (b) k_{1p} changes from 4 to 3.

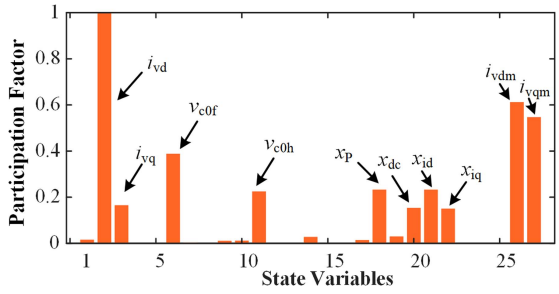

Fig. 18. Participation factors of the dominant root when $k_{1p} = 3$.

TABLE IV
PARAMETER OF THE EXPERIMENTAL SYSTEM

Circuit Parameter of Hybrid MMC					
V_s /V	50	L_t /mH	6	R_a /Ω	1
L_s /mH	6	L_a /mH	6	SM No. (FBSM/HBSM)	3/1
R_s /Ω	1	V_{dcn} /V	60	C_{sm} /μF	2160

As for Fig. 16, the root locus exhibits a similar trend to that of Fig. 16. However, the value of the critical dominant root is different due to the use of improved AAVM. As can be observed in Fig. 16, the critical value of k_{1p} is around 3.12, which means that the test system based on improved AAVM will become stable as k_{1p} increases over 3.12. In Fig. 16, the eigenvalue of the dominant root for $k_{1p} = 3.13$ are $-0.21 \pm j109.44$ and $k_{1p} = 3$ are $2.26 \pm j107.77$, which will be further verified by simulation in PSCAD.

To validate the correctness and accuracy of the root locus, the stability of the test system in PSCAD with different k_{1p} is tested. The control parameters of ac current inner loop PI are set as (4,100) initially and k_{1p} changes from 4 to 3 and 3.13 at $t = 2$ s, respectively. The dynamics of active power are plotted in Fig. 17.

It can be seen from Fig. 17(a) that the test system still remains asymptotically stable as k_{1p} changes from 4 to 3.13 at 2 s. The real part of the eigenvalue for $k_{1p} = 3.13$ is 0.15 in Fig. 15 which is inconsistent with the stability of the test system. Meanwhile, the real part of the eigenvalue for $k_{1p} = 3.13$ is -0.21 in Fig. 16 which means the root locus of improved AAVM can predict the stability of the test system correctly. As Fig. 17(b) shows, the dynamics of active power become unstable and the oscillating period is 0.057 s when k_{1p} changes from 4 to 3 at 2 s. The root locus in Figs. 15 and 16 can predict the stability of the test system correctly when k_{1p} changes from 4 to 3. The oscillation period corresponding to the unstable mode in Fig. 16 is $2\pi/107.77 = 0.0583$ s while the oscillation period corresponding to the unstable mode in Fig. 15 is $2\pi/105.24 = 0.0597$ s. The oscillation period of the small-signal model based on improved AAVM is much closer to the DSM. Figs. 15 and 16 validate the correctness and accuracy of the proposed small-signal model of hybrid MMC based on improved AAVM in the aspect of stability prediction and oscillating period. On the contrary, the conventional AAVM may cause the wrong assessment of the stability of hybrid MMC.

Fig. 18 illustrates the normalized participation factors of the unstable dominant root for $k_{1p} = 3$ in Fig. 16, where the highest participation factor is considered as the base value, and the magnitude of each participation factor is divided by the base value. The participation factors are calculated according to their definition in [24]. As can be seen in Fig. 18, the major contributors to the dominant modes in Fig. 17 are mainly related to the ac current, including the following:

1) the FF-dq components of ac current (i_{vd} and i_{vq});
2) the dc components of SM capacitor voltages (v_{c0f} and v_{c0h});
3) state variables of controllers (x_P, x_{dc}, x_{id}, x_{iq});
4) the measurements (i_{vdm} and i_{vqm}).

It can be concluded that ac current is the main reason for the instability of the system when $k_{1p} = 3$. The small signal stability of the system can be improved by adjusting the PI parameters of the current inner loop controller.

VII. EXPERIMENTAL VERIFICATION

In this section, a scaled-down hybrid MMC prototype is used to validate the correctness of the improved AAVM. The prototype and the circuit of the prototype are shown in Fig. 19(a) and (b), respectively. Each arm of the prototype contains an HBSM and three FBSMs. The power hardware of the SM is IGBT with freewheeling diodes and the physical diagram of SM is shown in Fig. 19(c). The three-phase converter connects to an ac voltage source via ac resistance and a dc voltage source. The converter is controlled to supply power to the dc source. The main parameters of the experimental system are listed in Table IV. The converter is modulated using the CPS-PWM technique with a carrier frequency of 500 Hz and the grid frequency is 50 Hz. This section also constructs the improved and conventional AAVM of the experimental system in PSCAD.

Figs. 20 and 21 show the steady-state performance of experimental results and simulation results of improved AAVM and conventional AAVM under $m_d = 1.33$, respectively. It can be observed that the shape of SM capacitor voltages in Fig. 20 are consistent with that of improved AAVM in Fig. 21. Besides, the FBSM and HBSM capacitance voltages in Fig. 20 have a

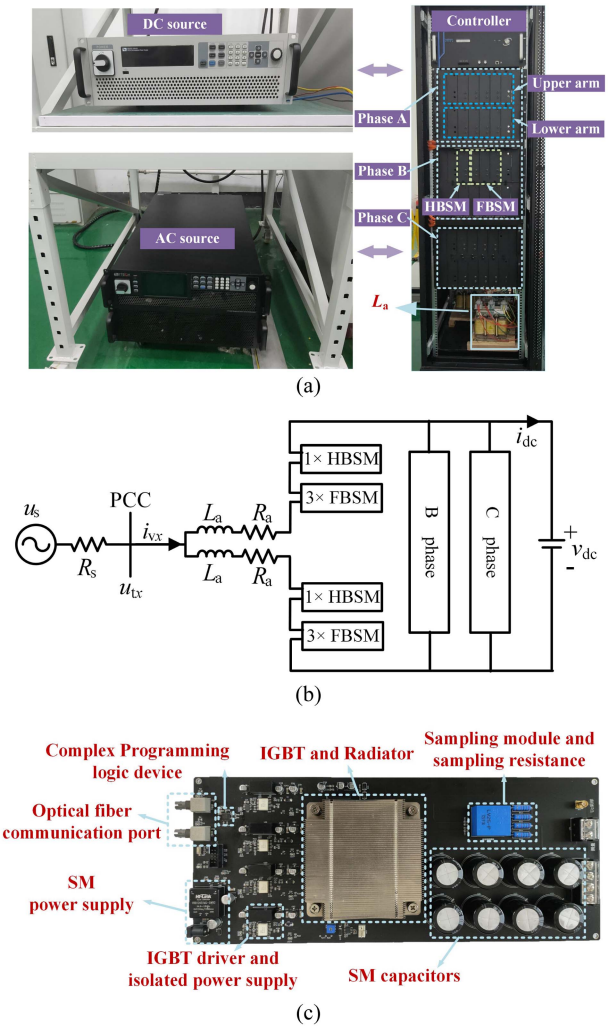

Fig. 19. Topology of experimental system. (a) Scale-down laboratory prototype. (b) Circuit of prototype. (c) Physical diagram of SM.

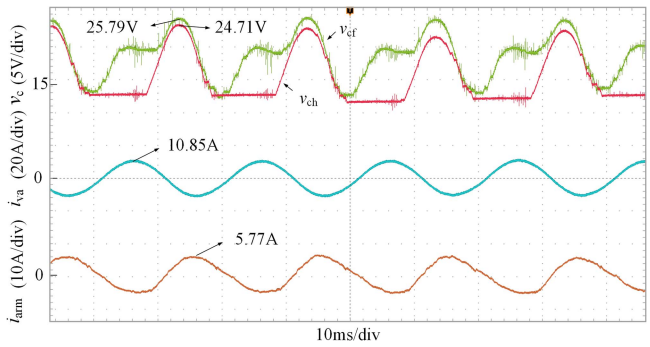

Fig. 20. Experimental results of the prototype at $m_d = 1.33$.

coincidence part in a period, which reconfirms the correctness of improved AAVM under the overmodulation mode.

In Figs. 20 and 21, the relative errors of the SM capacitor voltages between the experimental results and the simulation results of improved AAVM are 5.11% (FBSM) and 5.58% (HBSM), respectively. The simulation results of conventional AAVM have obvious errors compared with the experimental results. The

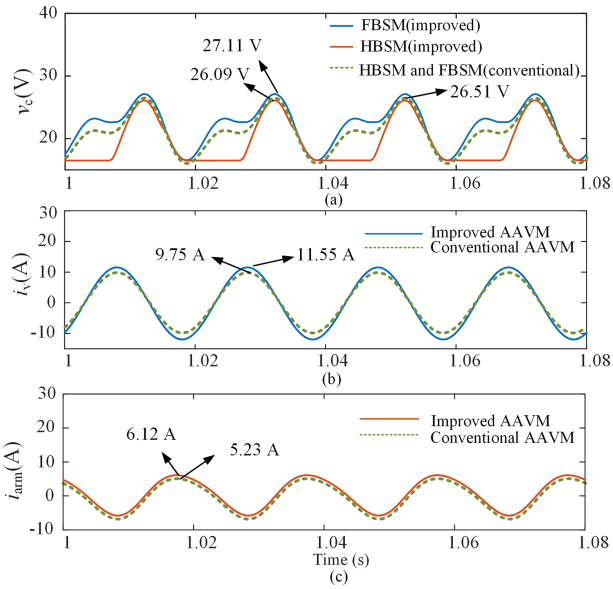

Fig. 21. Simulation results of the prototype at $m_d = 1.33$.

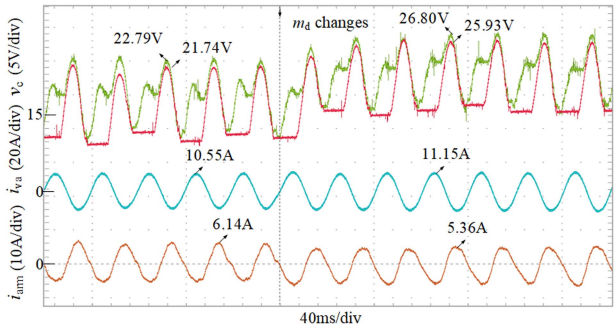

Fig. 22. Experimental results of the prototype when m_d changes.

reason for the error between experimental results and simulation results of improved AAVM is that the experimental system only contains four SMs and the improved AAVM does not consider the losses of the SMs. It can be concluded that the simulation results of improved AAVM are consistent with the experimental results.

Figs. 22 and 23 show the dynamic performance of the experimental and simulation results of improved AAVM and conventional AAVM when m_d changes from 1.67 to 1, respectively. It can be seen from Fig. 22 that the SM capacitor voltages increase and the capacitance voltages of FBSM and HBSM still have a coincidence part in a period. As for Fig. 23, the SM capacitor voltages, arm current and ac current of improved AAVM exhibit a similar trend to that of Fig. 22.

The steady-state value of capacitor voltages, arm current, and ac current of improved AAVM in the simulation results are consistent with that of the experimental results. The arm current and ac current of conventional AAVM also exhibit a similar trend with that of experimental results. However, the relative error of conventional AAVM is larger than that of improved AAVM. Therefore, the improved AAVM proposed in this article can reflect the dynamics of the experimental system correctly.

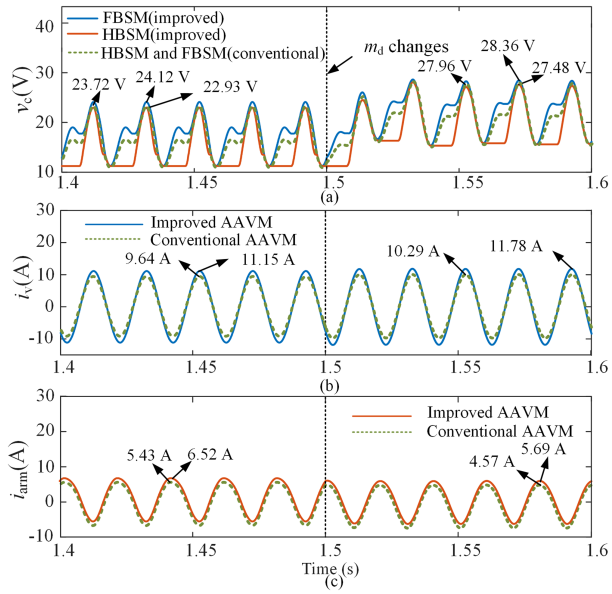

Fig. 23. Simulation results of the prototype when m_d changes at 1.5 s.

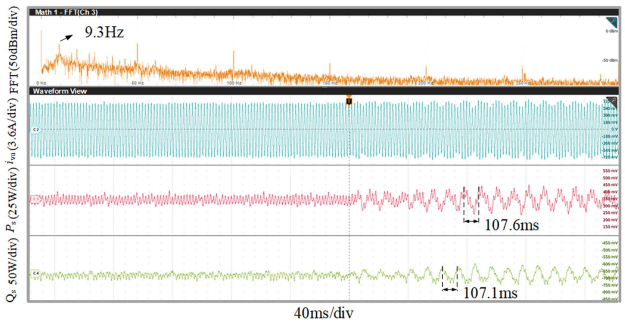

Fig. 24. Experimental results of the prototype when k_{1p} changes.

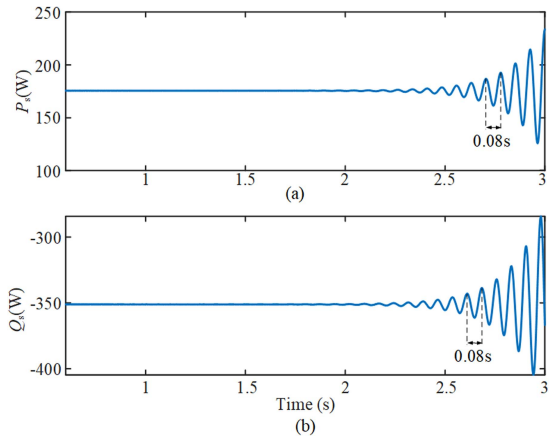

Fig. 25. Simulation results of the prototype when k_{1p} changes.

To verify the correctness of the small-signal model, the k_{1p} of the experimental system is changed from 4.5 to 0.45 in this section. Fig. 24 shows the experimental results of i_{va}, P_s, Q_s, and the spectrum of P_s. When k_{1p} changes, the experimental results show that the system oscillates, and the oscillation frequency of P_s is about 9.3 Hz. Besides, i_{va} contains frequency components of 40.7 and 59.3 Hz. According to the frequency coupling characteristics of MMC, it is also shown that the oscillation frequency of the experimental system is 9.3 Hz. Fig. 25 shows improved AAVM simulation results of P_s and Q_s of the prototype when k_{1p} changes from 4.5 to 0.45 at 1 s. As shown in Fig. 25, the oscillation frequency of improved AAVM is 1/0.08 = 12.5 Hz. The reason for the error of the oscillation frequency between experimental results and simulation results of improved AAVM is that the experimental system only contains four SMs and improved AAVM does not consider the losses, stray inductance, and capacitance of the SMs. Therefore, improved AAVM can reflect the oscillation dynamic performance of the experimental system correctly.

VIII. Conclusion

First, based on the difference in dynamic characteristics between FBSM and HBSM of hybrid MMC under negative voltage output conditions, this article presents the equivalent circuit of the improved AAVM and the arm reference voltage allocation algorithm which describes the nonlinear distribution of arm modulation signal between HBSM and FBSM. The complete improved AAVM is constituted by the equivalent circuit and the arm reference voltage allocation algorithm. Second, considering the higher harmonics of the capacitor voltages and the modulation signals, the dynamic differential equation of the electrical part and the nonlinear distribution in the *d*-*q* frame are derived. Based on the nonlinear allocation algorithm of the reference voltage and the piecewise solution method, the modular small-signal model of the hybrid MMC is established. Finally, the correctness of the proposed model is verified by simulation results. The simulation results show that the dynamics of the improved AAVM and the DSM are highly consistent under the negative voltage output condition, whereas the conventional AAVM has obvious errors. Besides, the simulation results validate the correctness of the small-signal model based on improved AAVM in the aspect of stability prediction while the conventional AAVM may cause the wrong assessment of stability. Meanwhile, the steady-state and dynamic operation experimental results confirm the correctness of the improved AAVM.

The improved AAVM has its limitations such as it could not simulate blocking conditions in practical applications. Improved AAVM uses a series of controlled voltage sources to simulate the arm output voltage of hybrid MMC. When the arm of hybrid MMC is blocked due to dc fault, submodule fault, and other reasons, the controlled voltage source is set to 0 directly without considering the influence of IGBT anti-parallel diode in SMs. Therefore, improved AAVM cannot simulate the current freewheeling process after blocking correctly. The improved AAVM cannot be used to simulate blocking conditions of the hybrid MMC. Besides, compared with the conventional AAVM, the improved AAVM slightly increases the simulation time, but the simulation efficiency is within the acceptable range according to Table II. Meanwhile, the accuracy of improved AAVM is higher than conventional AAVM significantly under overmodulation conditions, and the improved AAVM can reflect the stability of hybrid MMC correctly.

APPENDIX

The differential equations of internal differential currents are

$$\begin{aligned} L_a\frac{di_{\mathrm{dif0}}}{dt} =& -R_a i_{\mathrm{dif0}} - \frac{v_{\mathrm{dc}}}{2} + m_{0\mathrm{f}}v_{\mathrm{c0f}} \\ &+ \sum_{i=1}^{n}\frac{m_{\mathrm{idf}}v_{\mathrm{cidf}} + m_{\mathrm{iqf}}v_{\mathrm{ciqf}}}{2} \\ &+ m_{0\mathrm{h}}v_{\mathrm{c0h}} + \sum_{i=1}^{n}\frac{m_{\mathrm{idh}}v_{\mathrm{cidh}} + m_{\mathrm{iqh}}v_{\mathrm{ciqh}}}{2} \end{aligned} \tag{A1}$$

$$\begin{aligned} L_a\frac{di_{\mathrm{dif2d}}}{dt} =& -R_a i_{\mathrm{dif2d}} - 2\omega L_a i_{\mathrm{dif2q}} + \sum_{z=\mathrm{f,h}}\Bigg(m_{0\mathrm{z}}v_{\mathrm{c2dz}} \\ &+ m_{2\mathrm{dz}}v_{\mathrm{c0z}} + \frac{m_{1\mathrm{dz}}v_{\mathrm{c1dz}} - m_{1\mathrm{qz}}v_{\mathrm{c1qz}}}{2} \\ &+ \frac{m_{3\mathrm{dz}}v_{\mathrm{c1dz}} - m_{3\mathrm{qz}}v_{\mathrm{c1qz}}}{2} \\ &+ \frac{m_{4\mathrm{dz}}v_{\mathrm{c2dz}} - m_{4\mathrm{qz}}v_{\mathrm{c2qz}}}{2} \\ &+ \sum_{j=3}^{n}\Bigg(\frac{m_{(\mathrm{j}-2)\mathrm{dz}}v_{\mathrm{cjdz}}}{2} + \frac{s_{\mathrm{j}-2}s_{\mathrm{j}}m_{(\mathrm{j}-2)\mathrm{qz}}v_{\mathrm{cjqz}}}{2} \\ &+ \frac{m_{(\mathrm{j}+2)\mathrm{dz}}v_{\mathrm{cjdz}} + s_{\mathrm{j}+2}s_{\mathrm{j}}m_{(\mathrm{j}+2)\mathrm{qz}}v_{\mathrm{cjqz}}}{2}\Bigg)\Bigg) \end{aligned} \tag{A2}$$

$$\begin{aligned} L_a\frac{di_{\mathrm{dif2q}}}{dt} =& -R_a i_{\mathrm{dif2q}} + 2\omega L_a i_{\mathrm{dif2d}} + \sum_{z=\mathrm{f,h}}\Bigg(m_{0\mathrm{z}}v_{\mathrm{c2qz}} \\ &+ m_{2\mathrm{qz}}v_{\mathrm{c0z}} - \frac{m_{1\mathrm{qz}}v_{\mathrm{c1dz}} + m_{1\mathrm{dz}}v_{\mathrm{c1qz}}}{2} \\ &+ \frac{m_{3\mathrm{qz}}v_{\mathrm{c1dz}} + m_{3\mathrm{dz}}v_{\mathrm{c1qz}}}{2} \\ &- \frac{m_{4\mathrm{qz}}v_{\mathrm{c2dz}} + m_{4\mathrm{dz}}v_{\mathrm{c2qz}}}{2} \\ &+ \sum_{j=3}^{n}\Bigg(\frac{s_{\mathrm{j}-2}m_{(\mathrm{j}-2)\mathrm{qz}}v_{\mathrm{cjdz}}}{2} - \frac{s_{\mathrm{j}}m_{(\mathrm{j}-2)\mathrm{dz}}v_{\mathrm{cjqz}}}{2} \\ &+ \frac{-s_{\mathrm{j}+2}m_{(\mathrm{j}+2)\mathrm{dz}}v_{\mathrm{cjdz}} + s_{\mathrm{j}}m_{(\mathrm{j}+2)\mathrm{dz}}v_{\mathrm{cjqz}}}{2}\Bigg)\Bigg). \end{aligned} \tag{A3}$$

The dynamics of ac currents are

$$\begin{aligned} L_{\mathrm{e}}\frac{di_{\mathrm{vd}}}{dt} =& -R_{\mathrm{e}}i_{\mathrm{vd}} + v_{\mathrm{sd}} + \omega L_{\mathrm{e}}i_{\mathrm{vq}} + \sum_{z=\mathrm{f,h}}\Bigg(m_{0\mathrm{z}}v_{\mathrm{c1dz}} \\ &+ m_{1\mathrm{dz}}v_{\mathrm{c0}z} + \frac{m_{2\mathrm{dz}}v_{\mathrm{c1dz}} - m_{2\mathrm{qz}}v_{\mathrm{c1qz}}}{2} \\ &+ \sum_{j=2}^{n}\Bigg(\frac{m_{(\mathrm{j}-1)\mathrm{dz}}v_{\mathrm{cjdz}} + s_{\mathrm{j}-1}s_{\mathrm{j}}m_{(\mathrm{j}-1)\mathrm{qz}}v_{\mathrm{cjqz}}}{2} \\ &+ \frac{m_{(\mathrm{j}+1)\mathrm{dz}}v_{\mathrm{cjdz}} + s_{\mathrm{j}+1}s_{\mathrm{j}}m_{(\mathrm{j}+1)\mathrm{qz}}v_{\mathrm{cjqz}}}{2}\Bigg)\Bigg) \end{aligned} \tag{A4}$$

$$\begin{aligned} L_{\mathrm{e}}\frac{di_{\mathrm{vq}}}{dt} =& -R_{\mathrm{e}}i_{\mathrm{vq}} - \omega L_{\mathrm{e}}i_{\mathrm{vd}} + v_{\mathrm{sq}} + \sum_{z=\mathrm{f,h}}\Bigg(m_{0\mathrm{z}}v_{\mathrm{c1qz}} \\ &+ m_{1\mathrm{qz}}v_{\mathrm{c0}z} - \frac{m_{2\mathrm{qz}}v_{\mathrm{c1dz}} + m_{2\mathrm{dz}}v_{\mathrm{c1qz}}}{2} \\ &+ \sum_{j=2}^{n}\Bigg(\frac{m_{(\mathrm{j}-1)\mathrm{dz}}v_{\mathrm{cjqz}} - s_{\mathrm{j}}m_{(\mathrm{j}-1)\mathrm{qz}}v_{\mathrm{cjdz}}}{2} \\ &+ \frac{s_{\mathrm{j}+1}m_{(\mathrm{j}+1)\mathrm{qz}}v_{\mathrm{cjdz}} - s_{\mathrm{j}}m_{(\mathrm{j}+1)\mathrm{qz}}v_{\mathrm{cjqz}}}{2}\Bigg)\Bigg). \end{aligned} \tag{A5}$$

The dynamics of FBSM capacitor voltages are:

$$\begin{aligned} C_{\mathrm{eqF}}\frac{dv_{\mathrm{c0f}}}{dt} =& -\Bigg(m_{0\mathrm{f}}i_{\mathrm{dif0}} + \frac{m_{1\mathrm{df}}i_{\mathrm{vd}} + m_{1\mathrm{qf}}i_{\mathrm{vq}}}{4} \\ &+ \frac{m_{2\mathrm{df}}i_{\mathrm{dif2d}} + m_{2\mathrm{qf}}i_{\mathrm{dif2q}}}{2}\Bigg) \end{aligned} \tag{A6}$$

$$\begin{aligned} C_{\mathrm{eqF}}\frac{dv_{\mathrm{c1df}}}{dt} =& \omega C_{\mathrm{eqF}}v_{\mathrm{c1qf}} - \Bigg(\frac{m_{0\mathrm{f}}i_{\mathrm{vd}}}{2} + m_{1\mathrm{df}}i_{\mathrm{dif0}} + \frac{m_{1\mathrm{df}}i_{\mathrm{dif2d}}}{2} \\ &- \frac{m_{1\mathrm{qf}}i_{\mathrm{dif2q}}}{2} + \frac{m_{2\mathrm{df}}i_{\mathrm{vd}} - m_{2\mathrm{qf}}i_{\mathrm{vq}}}{4} \\ &+ \frac{m_{3\mathrm{df}}i_{\mathrm{dif2d}} + m_{3\mathrm{qf}}i_{\mathrm{dif2q}}}{2}\Bigg) \end{aligned} \tag{A7}$$

$$\begin{aligned} C_{\mathrm{eqF}}\frac{dv_{\mathrm{c1qf}}}{dt} =& -\omega C_{\mathrm{eqF}}v_{\mathrm{c1qf}} - \Bigg(\frac{m_{0\mathrm{f}}i_{\mathrm{vq}}}{2} + m_{1\mathrm{qf}}i_{\mathrm{dif0}} \\ &- \frac{m_{1\mathrm{qf}}i_{\mathrm{dif2d}}}{2} - \frac{m_{1\mathrm{df}}i_{\mathrm{dif2q}}}{2} - \frac{m_{2\mathrm{qf}}i_{\mathrm{vd}} + m_{2\mathrm{df}}i_{\mathrm{vq}}}{4} \\ &+ \frac{m_{3\mathrm{df}}i_{\mathrm{dif2q}} - m_{3\mathrm{qf}}i_{\mathrm{dif2d}}}{2}\Bigg) \end{aligned} \tag{A8}$$

$$\begin{aligned} C_{\mathrm{eqF}}\frac{dv_{\mathrm{c2df}}}{dt} =& -2\omega C_{\mathrm{eqF}}v_{\mathrm{c2qf}} - \Bigg(m_{0\mathrm{f}}i_{\mathrm{dif2d}} + m_{2\mathrm{df}}i_{\mathrm{dif0}} \\ &+ \frac{m_{1\mathrm{df}}i_{\mathrm{vd}}}{4} - \frac{m_{1\mathrm{qf}}i_{\mathrm{vq}}}{4} + \frac{m_{3\mathrm{df}}i_{\mathrm{vd}} - m_{3\mathrm{qf}}i_{\mathrm{vq}}}{4} \\ &+ \frac{m_{4\mathrm{df}}i_{\mathrm{dif2d}} - m_{4\mathrm{qf}}i_{\mathrm{dif2q}}}{2}\Bigg) \end{aligned} \tag{A9}$$

$$\begin{aligned} C_{\mathrm{eqF}}\frac{dv_{\mathrm{c2qf}}}{dt} =& 2\omega C_{\mathrm{eqF}}v_{\mathrm{c2df}} - \Bigg(m_{0\mathrm{f}}i_{\mathrm{dif2d}} + m_{2\mathrm{qf}}i_{\mathrm{dif0}} \\ &- \frac{m_{1\mathrm{qf}}i_{\mathrm{vd}}}{4} - \frac{m_{1\mathrm{df}}i_{\mathrm{vq}}}{4} + \frac{m_{3\mathrm{qf}}i_{\mathrm{vd}} + m_{3\mathrm{df}}i_{\mathrm{vq}}}{4} \\ &- \frac{m_{4\mathrm{qf}}i_{\mathrm{dif2d}} + m_{4\mathrm{df}}i_{\mathrm{dif2q}}}{2}\Bigg). \end{aligned} \tag{A10}$$

If $k \geq 3$

$$\begin{aligned} C_{\mathrm{eqF}}\frac{dv_{\mathrm{ckdf}}}{dt} =& s_{\mathrm{k}}k\omega C_{\mathrm{eqF}}v_{\mathrm{ckqf}} - \Bigg(m_{\mathrm{kdf}}i_{\mathrm{diff0}} + \frac{m_{(\mathrm{k}-1)\mathrm{df}}i_{\mathrm{vd}}}{4} \\ &- \frac{s_{\mathrm{k}-1}m_{(\mathrm{k}-1)\mathrm{qf}}i_{\mathrm{vq}}}{4} \\ &+ \frac{m_{(\mathrm{k}-2)\mathrm{df}}i_{\mathrm{dif2d}} + s_{\mathrm{k}-2}m_{(\mathrm{k}-2)\mathrm{qf}}i_{\mathrm{diff2q}}}{2} \\ &+ \frac{m_{(\mathrm{k}+1)\mathrm{df}}i_{\mathrm{vd}} + s_{\mathrm{k}+1}m_{(\mathrm{k}+1)\mathrm{qf}}i_{\mathrm{vq}}}{4} \\ &+ \frac{m_{(\mathrm{k}+2)\mathrm{df}}i_{\mathrm{dif2d}} - s_{\mathrm{k}+2}m_{(\mathrm{k}+2)\mathrm{qf}}i_{\mathrm{dif2q}}}{2}\Bigg) \end{aligned} \tag{A11}$$

$$C_{\mathrm{eqF}}\frac{dv_{\mathrm{ckqf}}}{dt} = -s_{\mathrm{k}}k\omega C_{\mathrm{eqF}}v_{\mathrm{ckdf}} - s_{\mathrm{k}}\Bigg(s_{\mathrm{k}}m_{\mathrm{kqf}}i_{\mathrm{dif0}} + \frac{s_{\mathrm{k}-1}m_{(\mathrm{k}-1)\mathrm{qf}}i_{\mathrm{vd}}}{4} + \frac{m_{(\mathrm{k}-1)\mathrm{df}}i_{\mathrm{vq}}}{4} + \frac{s_{\mathrm{k}-2}m_{(\mathrm{k}-2)\mathrm{qf}}i_{\mathrm{dif2d}} - m_{(\mathrm{k}-2)\mathrm{df}}i_{\mathrm{dif2q}}}{2} + \frac{s_{\mathrm{k}+1}m_{(\mathrm{k}+1)\mathrm{qf}}i_{\mathrm{vd}} - m_{(\mathrm{k}+1)\mathrm{df}}i_{\mathrm{vq}}}{4} + \frac{s_{\mathrm{k}+2}m_{(\mathrm{k}+2)\mathrm{qf}}i_{\mathrm{dif2d}} + m_{(\mathrm{k}+2)\mathrm{df}}i_{\mathrm{dif2q}}}{2}\Bigg). \tag{A12}$$

The expression of HBSM capacitor voltages can be obtained by replacing the subscript "f" with "h."

REFERENCES

[1] S. Debnath, J. Qin, B. Bahrani, M. Saeedifard, and P. Barbosa, "Operation, control, and applications of the modular multilevel converter: A review," *IEEE Trans. Power Electron.*, vol. 30, no. 1, pp. 37–53, Jan. 2015.

[2] G. Song, J. Hou, B. Guo, K. S. T. Hussain, T. Wang, and B. Masood, "Active injection for single-ended protection in DC grid using hybrid MMC," *IEEE Trans. Power Del.*, vol. 36, no. 3, pp. 1651–1662, Jun. 2021.

[3] S. Xu et al., "Dynamic model of the dc fault clearing process of a hybrid modular multilevel converter considering commutations of the fault current," *IEEE Trans. Power Electron.*, vol. 35, no. 7, pp. 6668–6672, Jul. 2020.

[4] R. Li, L. Xu, L. Yu, and L. Yao, "A hybrid modular multilevel converter with reduced full-bridge submodules," *IEEE Trans. Power Del.*, vol. 35, no. 4, pp. 1876–1885, Aug. 2020.

[5] R. Zeng, L. Xu, L. Yao, and B. W. Williams, "Design and operation of a hybrid modular multilevel converter," *IEEE Trans. Power Electron.*, vol. 30, no. 3, pp. 1137–1146, Mar. 2015.

[6] J. Qin, M. Saeedifard, A. Rockhill, and R. Zhou, "Hybrid design of modular multilevel converters for HVDC systems based on various submodule circuits," *IEEE Trans. Power Del.*, vol. 30, no. 1, pp. 385–394, Feb. 2015.

[7] C. Zhao, Y. Li, Z. Li, P. Wang, X. Ma, and Y. Luo, "Optimized design of full-bridge modular multilevel converter with low energy storage requirements for HVdc transmission system," *IEEE Trans. Power Electron.*, vol. 33, no. 1, pp. 97–109, Jan. 2018.

[8] Y. Zhang, Y. Zhang, J. Zhang, F. Deng, and F. Blaabjerg, "Design analysis and capacitance reduction of hybrid modular multilevel converters under boost ac mode," *IEEE Trans. Power Electron.*, vol. 38, no. 12, pp. 14918–14929, Dec. 2023.

[9] E. Shahriari, F. Gruson, P. Vermeersch, P. Delarue, F. Colas, and X. Guillaud, "A novel dc fault ride through control methodology for hybrid modular multilevel converters in HVDC systems," *IEEE Trans. Power Del.*, vol. 35, no. 6, pp. 2831–2840, Dec. 2020.

[10] C. Liu, F. Deng, Q. Heng, X. Cai, R. Zhu, and M. Liserre, "Crossing thyristor branches-based hybrid modular multilevel converters for dc line faults," *IEEE Trans. Ind. Electron.*, vol. 68, no. 10, pp. 9719–9730, Oct. 2021.

[11] V. Psaras, D. Vozikis, G. P. Adam, and G. Burt, "DC fault management strategy for continuous operation of HVDC grids based on customized hybrid MMC," *IEEE J. Emerg. Sel. Topics Power Electron.*, vol. 9, no. 6, pp. 7099–7111, Dec. 2021.

[12] S. Cui and S. K. Sul, "A comprehensive DC short-circuit fault ride through strategy of hybrid modular multilevel converters (MMCs) for overhead line transmission," *IEEE Trans. Power Electron.*, vol. 31, no. 11, pp. 7780–7796, Nov. 2016.

[13] J. H. Lee, J. J. Jung, and S. K. Sul, "Balancing of submodule capacitor voltage of hybrid modular multilevel converter under DC-bus voltage variation of HVDC system," *IEEE Trans. Power Electron.*, vol. 34, no. 11, pp. 10458–10470, Nov. 2019.

[14] Y. Zhang, J. Zhang, and F. Deng, "Improved CPS-PWM approach for over-modulation operations of hybrid modular multilevel converter," *IEEE J. Emerg. Sel. Topics Power Electron.*, vol. 10, no. 5, pp. 5933–5943, Oct. 2022.

[15] S. Lu, L. Yuan, K. Li, and Z. Zhao, "An improved phase-shifted carrier modulation scheme for a hybrid modular multilevel converter," *IEEE Trans. Power Electron.*, vol. 32, no. 1, pp. 81–97, Jan. 2017.

[16] P. D. Judge, G. Chaffey, M. M. C. Merlin, P. R. Clemow, and T. C. Green, "Dimensioning and modulation index selection for the hybrid modular multilevel converter," *IEEE Trans. Power Electron.*, vol. 33, no. 5, pp. 3837–3851, May 2018.

[17] T. Bandaru, D. Samajdar, P. B. S. Varma, T. Bhattacharya, and D. Chatterjee, "Optimum injection of second harmonic circulating currents for balancing capacitor voltages in hybrid MMC during reduced DC voltage conditions," *IEEE Trans. Ind. Appl.*, vol. 56, no. 2, pp. 1649–1660, Mar./Apr. 2020.

[18] Y. Dong, J. Tang, H. Yang, W. Li, and X. He, "Capacitor voltage balance control of hybrid modular multilevel converters with second-order circulating current injection," *IEEE J. Emerg. Sel. Topics Power Electron.*, vol. 7, no. 1, pp. 157–167, Mar. 2019.

[19] R. Vidal-Albalate and J. Forner, "Modeling and enhanced control of hybrid full bridge–Half bridge MMCs for HVDC grid studies," *Energies*, vol. 13, no. 1, Jan. 2020, Art. no. 180.

[20] X. Lu, W. Xiang, W. Lin, and J. Wen, "State-space model and PQ operating zone analysis of hybrid MMC," *Electr. Power Syst. Res.*, vol. 162, pp. 99–108, Sep. 2018.

[21] Q. Hao, Z. Li, C. Yue, F. Gao, and S. Wang, "Small-signal model and dynamics of MMC-HVDC grid under unbalanced grid conditions," *IEEE Trans. Power Del.*, vol. 36, no. 5, pp. 3172–3184, Oct. 2021.

[22] W. Lin, D. Jovcic, S. Nguefeu, and H. Saad, "Full-bridge MMC converter optimal design to HVDC operational requirements," *IEEE Trans. Power Del.*, vol. 31, no. 3, pp. 1342–1350, Jun. 2016.

[23] M. Feng, Y. Guo, J. Xu, and C. Zhao, "Start-up control strategies of hybrid MMC and configuration of FBSM," *J. North China Electr. Power Univ.*, vol. 44, no. 6, pp. 28–35, Nov. 2017.

[24] P. Kundur, *Power System Stability and Control*. New York, NY, USA: McGraw-Hill, 1994, pp. 707–716.

Meng Guo received the B.E. degree in electrical engineering from Jilin University, Changchun, China, in 2020. He is currently working toward the Ph.D. degree in modeling, small-signal stability analysis and control of MMC with the School of Electrical Engineering, Shandong University, Jinan, China.

His research interests include modeling and small-signal stability analysis of HVdc grids.

Quanrui Hao (Member, IEEE) received the B.E. degree in electrical engineering from Tianjin University, Tianjin, China, in 2006, the M.E. degree in electrical engineering from Zhejiang University, Hangzhou, China, in 2008, and the Ph.D. degree in electrical engineering from McGill University, Montreal, QC, Canada, in 2013.

Since 2014, he has been with the Department of Electrical Engineering, Shandong University, Jinan, China, where he is currently a Full Professor. His research interests include modular multilevel converters, FACTS, and renewable energy integration through HVdc.

Lei Ding (Senior Member, IEEE) received the B.E. and Ph.D. degrees in electrical engineering from Shandong University, Jinan, China, in 2001 and 2007, respectively.

From 2008 to 2009, he was a Postdoctoral Researcher with Tsinghua University. From 2010 to 2011, he was a Research Associate with The University of Manchester. He is currently a Professor with Shandong University. He is currently an Associate Editor for the *International Journal of Electrical Power & Energy Systems*. His research interests include low inertia systems, integration of renewable energy, and power system wide-area protection.